Functional specialization within the inferior parietal lobes across cognitive domains

Short title: Specialization in the inferior parietal cortex

Ole Numssen[1], Danilo Bzdok[2,3,†,*], Gesa Hartwigsen[1,†,*]

[1] Lise Meitner Research Group "Cognition and Plasticity", Max Planck Institute for Human Cognitive and Brain Sciences Leipzig, Germany

[2] Department of Biomedical Engineering, McConnell Brain Imaging Centre, Montreal Neurological Institute, Faculty of Medicine, McGill University, Montreal, Canada

[3] Mila - Quebec Artificial Intelligence Institute, Montreal, Canada

[†] shared senior authorship

Main text: 4539 words
Materials and Methods: 3201 words
Abstract: 150 **words**

Number of Figures: 5**; Number of Tables:** 2

*Correspondence should be addressed to:

Danilo Bzdok
McConnell Brain Imaging Centre
Department of Biomedical Engineering
Montreal Neurological Institute
3801 rue University
Bureau #872D
Montréal (Québec) H3A 2B4, Canada
Phone: +1 438 524 2713
danilo.bzdok@mcgill.ca

Gesa Hartwigsen
Lise Meitner Research Group
Cognition and Plasticity
Max Planck Institute for Human
Cognitive and Brain Sciences
Stephanstrasse 1a
D-04103 Leipzig, Germany
Phone: +49 341 9940162
hartwigsen@cbs.mpg.de

1 **Abstract**

2 The inferior parietal lobe (IPL) is a key neural substrate underlying diverse mental processes, from

3 basic attention to language and social cognition, that define human interactions. Its putative domain-

4 global role appears to tie into poorly understood differences between cognitive domains in both

5 hemispheres. Across attentional, semantic, and social cognitive tasks, our study explored functional

6 specialization within the IPL. The task specificity of IPL subregion activity was substantiated by

7 distinct predictive signatures identified by multivariate pattern-learning algorithms. Moreover, the

8 left and right IPL exerted domain-specific modulation of effective connectivity among their

9 subregions. Task-evoked functional interactions of the anterior and posterior IPL subregions involved

10 recruitment of distributed cortical partners. While anterior IPL subregions were engaged in strongly

11 lateralized coupling links, both posterior subregions showed more symmetric coupling patterns across

12 hemispheres. Our collective results shed light on how under-appreciated functional specialization in

13 the IPL supports some of the most distinctive human mental capacities.

14

1

Introduction

18 Many cognitive processes are realized by spatially distributed neural networks in the human brain.

19 The inferior parietal lobe (IPL) is a heteromodal convergence zone of various brain networks that is

20 central to realizing key cognitive operations across different levels of the neural processing hierarchy

21 (Kernbach et al., 2018; Seghier, 2013). These mental operations include lower-level processes, such

22 as spatial attention, as well as higher-level processes that are distinctly elaborate in the human species,

23 like semantic memory and modes of social exchange.

24   During primate evolution, the IPL has probably undergone remarkable expansion and

25 functional reorganization (Van Essen & Dierker, 2007; Xu et al., 2020). The emergence of new areas

26 inside the human IPL has been seriously considered (Mars et al., 2013), while its precise

27 correspondence to nonhuman homologues is still debated (Seghier, 2013). The evolutionary

28 trajectory of the IPL, as part of the recent cortical expansion in humans may bear important

29 relationships to language ability, future planning, problem solving, and other complex mental

30 operations (Seghier, 2013) at which humans excel.

31   Diverse cognitive capacities have been linked to neural activity in the IPL. Among these,

32 spatial attention is crucial in an ever-changing environment that requires rapid behavioral adaptation

33 (Corbetta et al., 2008). Systematic reviews have identified the right IPL as a key region for

34 visuospatial attention (Corbetta et al., 2008). Accordingly, neurological damage of the right IPL

35 entails a clinical condition called hemi-neglect: the failure to orient visual attention to the

36 contralesional side (Morrow & Ratcliff, 1998). In contrast to visuospatial attention, language function

37 is widely accepted to lateralize to the (dominant) left hemisphere (Friederici, 2017). Tissue damage

38 to the left temporo-parietal cortex has been reported, for decades, to cause impairments of semantic

39 processing – key to reading and other elaborate forms of language comprehension (Binder et al.,

40 2009; Hartwigsen et al., 2016; Seghier, 2013). Semantic processing is instrumental for the human

41 ability to contextualize and act according to the meaning of objects, events, and situations (Lambon

42 Ralph & Patterson, 2008).

43   Moreover, semantic concepts are an integral component of numerous high-level cognitive

44   operations, and are suspected to contribute to both social cognition and language from early

45   development to adulthood (Binder & Desai, 2011). Semantic processing is presumably closely

46   intertwined with social cognition. This view receives support from previous reports on spatial overlap

47   between both cognitive domains in the left IPL (Bzdok et al., 2016; Mars et al., 2011; Seghier, 2013).

48   However, many human neuroimaging experiments have shown that advanced social cognitive

49   functions, such as the capacity to infer others' thoughts, beliefs, and behavioral dispositions, tend to

50   engage the IPL in both hemispheres (Bzdok et al., 2016).

51   Substantiating these earlier hints at functional specialization of left versus right IPL, both

52   regions also differ on the structural level. Architectural heterogeneity is indicated by cytoarchitectonic

53   borders and gyral differentiation (Caspers et al., 2008) as well as anatomical fiber bundle connections

54   as quantified by fiber tractography (Caspers et al., 2011). Such heterogeneity in the IPL is not only

55   found between individuals, but also between the left and right hemisphere (Toga & Thompson, 2003).

56   This structural scaffold has the potential to support the unique neurocognitive properties of the left

57   and right IPL.

58   Finally, the IPL harbors a major hub of the transmodal association network (Braga et al., 2019)

59   ('default mode network') and is densely connected with other cortical key areas for various functions.

60   This is reflected in intimate functional interactions with several other large-scale brain networks as

61   measured by intrinsic functional connectivity (Buckner & DiNicola, 2019). Despite indications in

62   favor of lateralized functional specialization for human-defining cognitive domains, it remains

63   unclear how the left and right IPL interact with distributed neural networks to realize advanced

64   cognitive operations like social and semantic processes.

65   For these reasons, our study capitalized on cognitive neuroimaging experiments that tap on

66   multiple functional domains. The combination of an arsenal of data-driven analysis techniques

67   allowed zooming in on the functional specialization and brain-wide interaction profiles of the IPL

68   and its segregated components. Our well-matched experimental paradigms prompted attentional

69   reorienting, lexical decisions, and mental perspective taking – archetypical processes that exemplify

70   the broader cognitive domains attention, semantics, and social cognition. The direct task comparison

71   in the same sample of subjects enabled us to identify functional specialization and involvement of

72   common mechanisms across attentional, semantic, and social realms of human cognition. Our unique

73   characterization of IPL function, subspecialization, and interaction patterns provides key insights into

74   cognitive operations that underlie elaborate forms of human interaction and communication.

Results

76   **IPL recruitment in different cognitive tasks: neural activity responses**

77   We designed three different tasks to probe the three domains of interest. An attentional reorienting

78   task required subjects to make spatially congruent button presses in response to visually presented

79   cues. A lexical decision task probed visual word-pseudoword decisions and a mental perspective

80   taking task prompted decisions on the mental beliefs of others (Fig. S1 for the experimental design

81   and behavioral results).

82   We first examined neural activity responses for each task separately by contrasting each target

83   condition (*invalid*, *word*, *false belief*) with its respective control condition (*valid*, *pseudoword*, *true*

84   *belief*). In this analysis, all tasks showed increased neural activity in a widespread set of brain regions,

85   including the IPL.
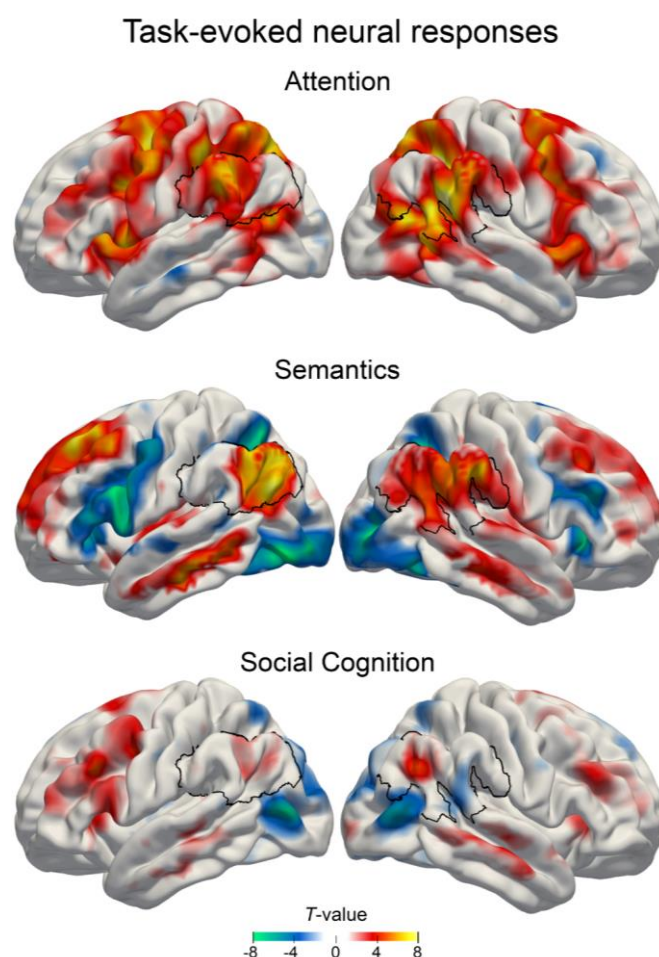
86   *Attentional reorienting task*

87   Relative to the control condition, we found that the attentional reorienting condition significantly

88   modulated neural activity in several nodes of the default mode network, including the right inferior

89   parietal lobes (IPL) (supramarginal gyrus) and to a lesser extent also the left IPL (supramarginal

90   gyrus), as well as the bilateral precuneus. Key nodes of the dorsal attention network were also

91   activated, including the left frontal eye field and superior parietal lobe.

4

92   *Lexical decision task*

93   Compared to pseudoword processing, real word processing predominantly activated left-hemispheric

94   parts of the default mode network, including the IPL (angular gyrus) and middle cingulate gyrus, as

95   well as the superior frontal gyrus.

96   *Social cognition task*

97   As expected, the results for the social cognition task were less strong (Rothmayr et al., 2011; Sommer

98   et al., 2010). Uncorrected peak activations for the false belief relative to the true belief task

99   encompassed bilateral areas, including the supplementary motor cortex, inferior frontal gyrus and

100   precentral gyrus. To a lesser extent, nodes of the default mode network were also engaged, including

101   the left precentral gyrus, right IPL (angular gyrus), and bilateral precuneus.

102

103   **Fig. 1. Main effects of estimated neural activity in the three cognitive domains.** Task-dependent BOLD

104   responses were quantified using common mass-univariate analyses at the whole-brain level. **Attentional**

105   **reorienting task.** *invalid > valid* contrast. **Semantic task.** *word > pseudoword* contrast. **Social cognition task.**

106   *false belief > true belief* contrast. Colors indicate unthresholded T-values for display purposes. Warm colors:

107   higher GLM beta estimates for the target conditions. Cold colors: higher GLM beta estimates for the control

108   condition.   Black   outline: region   of   interest   in   the   inferior   parietal   lobe.

109   Experimental design and behavioral results: Figure 1–figure supplement 1

110   For details on task-specific activity patterns, see Fig. 1 and Table S1.

111   To summarize neural activity responses in the IPL, we found strong upregulation of the right

112   supramarginal gyrus (x, y, z = 57, -48, 24; T = 9.68) during attentional reorienting, left angular gyrus

113   (x, y, z = -51, -72, 28; T = 8.00) during lexical decisions, and right angular gyrus (51, -60, 31; T =

114   5.15) during perspective taking. Standard mass-univariate analyses showed that all three tasks

115   recruited areas within the larger IPL region in at least one hemisphere.

116   **Functional parcellation of the IPL in two subregions**

117   To isolate coherent structure-function mappings from neural task responses, we used data-driven

118   clustering algorithms to separate the cytoarchitectonically constrained region of interest (ROI) in the

119   IPL into subregions (see Methods for details). According to the applied cluster validity criteria, a two-

120   cluster solution was indicated to be optimal in each hemisphere considering different cluster numbers.

121   The choice of two final clusters was based on majority votes yielding 97.1% and 78.8% agreement

122   across 25 distinct cluster validity criteria (cf. Methods) for left and right IPL, respectively (Table 1).

123   The three-cluster solution emerged as the second best choice (left IPL: 2.8% agreement, right IPL:

124   21.2% agreement).

125   To investigate the possible influence of general motor responses within the IPL on our results, we

126   estimated a third set of GLMs ($GLM_{cond+RT}$), which was based on the initial GLM_{cond} with one

127   additional regressor that modeled reaction times for all three tasks. This reaction time regressor

128   captured unspecific motor preparation and execution components that were not of interest here. The

129   task-dependent BOLD responses closely resembled the results from the original analysis (Figure 3–

130   figure supplements 2). The data-driven clustering based on these results selected a similar parcellation

6

131   solution with comparable certainty. 95.3% and 73.0% of the majority votes selected a two cluster

132   solution for the left and right IPL respectively, based on $GLM_{cond+RT}$. 82 voxels in the left IPL and 73

133   in the right IPL were unstable across random initializations. The cluster similarity across solutions is

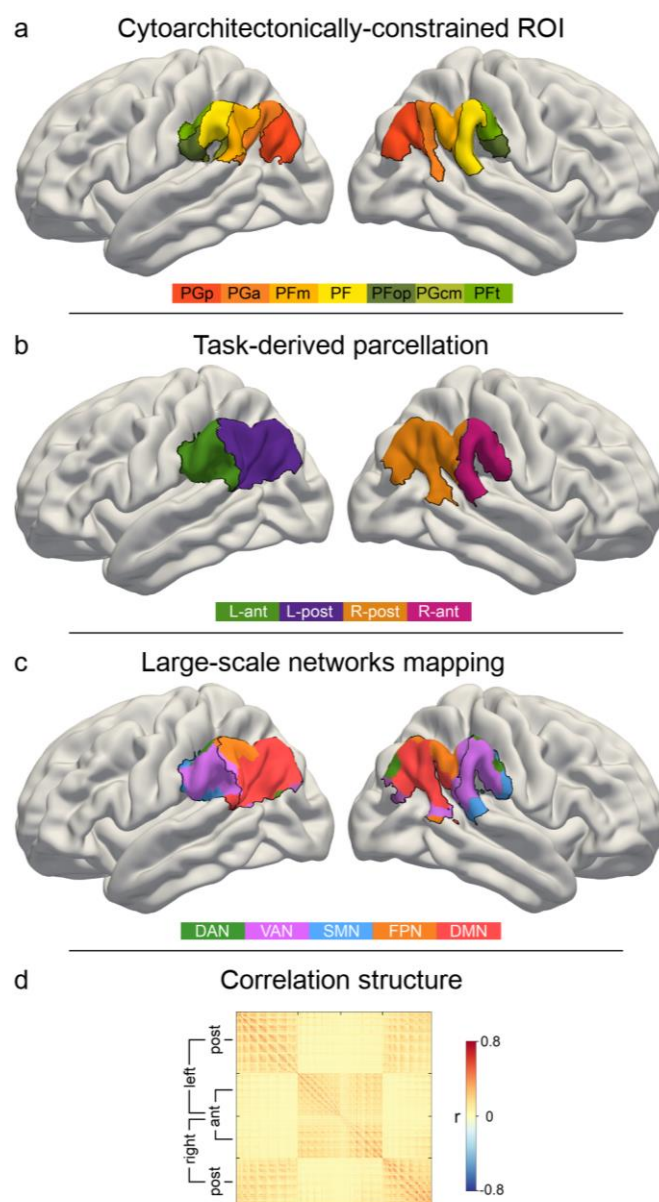134   illustrated in Figure 3–figure supplement 3.

135

136   **Fig. 2. IPL parcellation extracted from neural activity responses across attention, semantics, and social**

137   **cognition.** Neural activity estimates from all three task experiments were pooled to achieve a data-driven

138   segregation of the inferior parietal lobe, separately in each hemisphere. **(a)** Cytoarchitectonic boundaries

139   defined the contours of our region of interest (ROI) (Zilles & Amunts, 2010). **(b)** The derived ROI was

140   submitted to automatic parcellation into subregions to capture neural activity profiles of the three domains in

141   each hemisphere. L-ant: left anterior subregion. L-post: left posterior subregion. R-ant: right anterior

142   subregion. R-post: right posterior subregion. **(c)** Mapping of large-scale brain networks (Yeo et al., 2011) to

143   the ROI. Posterior subregions are predominantly populated by the default mode network (DMN), while the

7

144 anterior regions mainly host the ventral attention network (VAN). DAN: dorsal attention network. FPN: fronto-
145 parietal network. SMN: somatomotor network. **(d)** Similarity matrix of voxel-wise neural activity estimates of
146 single trials, reordered according to (c). The similarity structure reproduces the parcellation results.

147 Hemispheric symmetry of the final IPL parcellation: Figure 2–figure supplement 1
148 Task-evoked neural responses in the IPL with explicit motor preparation modelling: Figure 2–figure
149 supplement 2
150 Explicitly modelling motor preparation yields a similar clustering solution: Figure 2–figure supplement 3

151 For all later analysis steps, 74 (out of 1102) voxels in the left and 84 (out of 1123) in the right
152 IPL ROI were removed from the final solution because their cluster assignments were unstable across
153 the random centroid initializations of the k-means algorithm. All discarded voxels were located at the
154 cluster borders. The IPL parcellation procedure led to one anterior subregion (left hemisphere: L-ant,
155 right hemisphere: R-ant) and one posterior subregion (L-post, R-post) in each hemisphere (Fig. 2B).

156 Hemispheric asymmetries in cluster assignment were evaluated by quantifying topographical
157 overlap after flipping the right-left axis of the four derived IPL subregions (Fig. S3). Around two
158 thirds of the voxels composing the IPL ROI (left: 64.98%, right: 66.31%) were spatially congruent
159 across hemispheres. Considering these corresponding voxels contained in both left and right IPL ROI,
160 subregion-specific across-hemisphere congruency was nearly perfect (L-ant: 88.97%; L-post: 100%;
161 R-ant: 100%; R-post: 93.48%). The data-driven IPL parcellation into two subregions in each
162 hemisphere served as the basis for all subsequent analyses.

163

164

165 **Table 1. Task-derived IPL subregions**

Hemisphere	Position	Label	Volume	Center of mass	Cytoarchitectonic area
Left	anterior	L-ant	11.6 cm^3	-57, -32, 30	PF, PFop, PGcm, PFt
Left	posterior	L-post	20.7 cm^3	-48, -61, 33	PGa, PGp, PFm, PF
Right	anterior	R-ant	12.9 cm^3	58, -29, 28	PF, PFop, PGcm, PFt
Right	posterior	R-post	19.8 cm^3	51, -57, 32	PGa, PGp, PFm

166 *Note:* Cytoarchitectonic assignment was performed with the SPM Anatomy Toolbox. Center of mass
167 is given in MNI coordinates (x, y, z).

Task activity responses are predictive for different cognitive domains

Building on the obtained functional parcellation of the IPL into two core subregions that show different activation patterns for the probed cognitive domains, we investigated task-dependent specialization of IPL function using tools from machine learning. By deploying a linear predictive pattern-learning algorithm, we solved the classification problem of assigning task-membership from single experimental trials based on the subregion-level neural activity changes. We evaluated the quality of the predictive model via leave-one-subject-out cross-validation, that is, by testing the fitted model on data from a subject that was not used during model building. Our results indicate that neural activity response patterns from our IPL subregions alone carried relevant information that was granular enough to allow for successful task classification significantly above chance. The logistic predictive model was cross-validated in a one-versus-rest scheme to attempt classifying trial brain scans from hold-out subjects. This machine learning pipeline resulted in an overall out-of-sample classification accuracy of 52.11% (chance: 33.33%). Note that this cross-validation scheme leads to conservative accuracy estimates, as the classifier is tested on brain activity information from subjects it has not seen before. Therefore this approach provides a reliable estimate for the expected generalization in neuroimaging subjects scanned in the future (Bzdok & Yeo, 2017). Prediction accuracy reached 31.09% for the attentional reorienting task, 59.24% for the lexical decision task and 66.41% for the perspective taking task.

9

Predictive relevance of activity

Attention

Semantics

Social Cognition
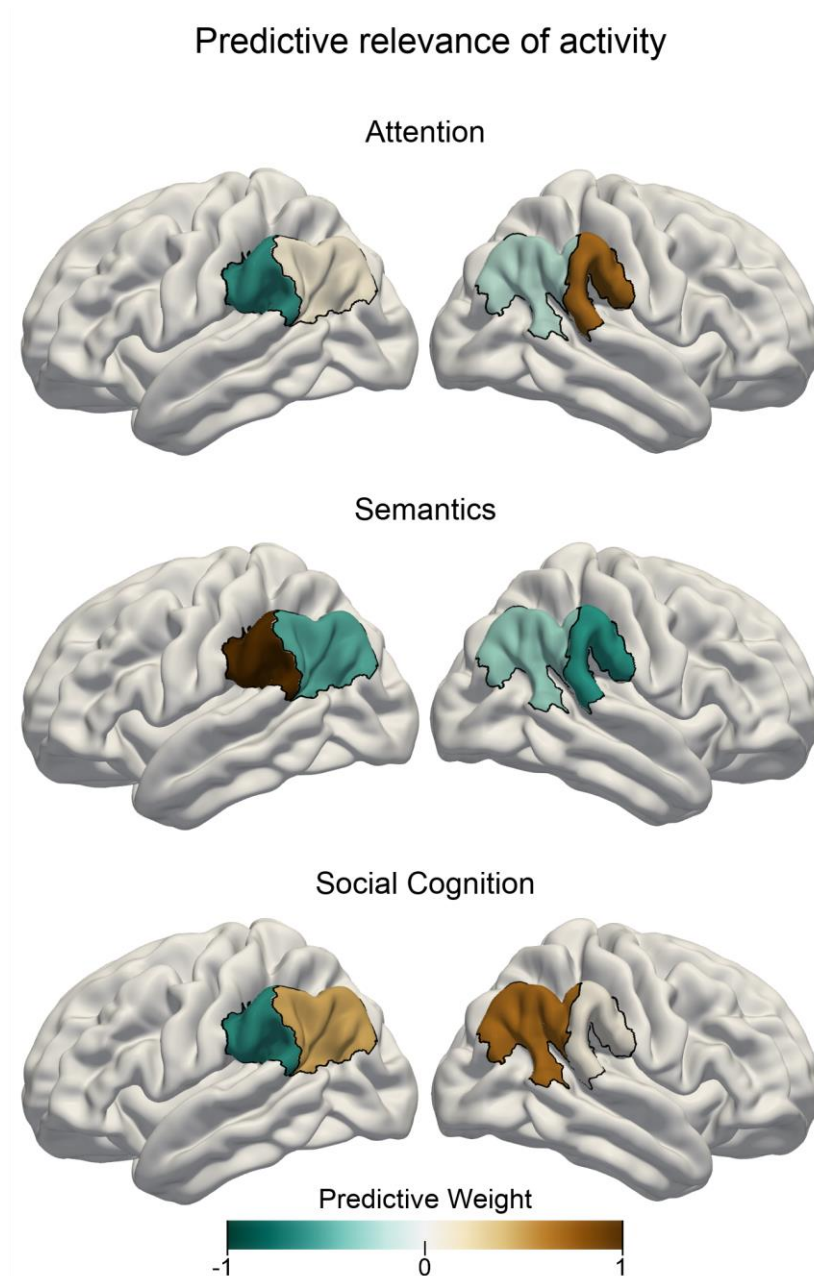
Predictive Weight

-1   0   1

186

Fig. 3. Task-specific predictive contributions of IPL subregions. Pattern-learning algorithms extracted predictive rules from neural activity estimates aggregated in the left vs. right anterior vs. posterior IPL subregions from the three target experimental conditions for attentional reorienting **(top)**, lexical decisions **(center)**, and perspective taking of others' mental states **(bottom)**. Colors show the predictive signature with relative contributions of each of the four IPL subregions in detecting the presence of the three cognitive states from neural activity responses. A more positive subregion weight (brown color) for a given task implies that neural activity from this subregion carried information that increased the probability of a specific task being represented in trial brain scans. A leave-one-subject-out cross-validation was implemented to fit the predictive model. Negative values (cold colors) denote driving the prediction decision towards the respective other tasks.

Figure 3–figure supplement 1. Neural activity estimates for the target and control conditions of the three tasks.

10

199   Relative to the other two experimental tasks, increased neural activity in the right anterior

200   subregion and less neural activity in the left anterior subregion was associated with the attentional

201   reorienting task when considering multivariate patterns distributed across all IPL subregions (see Fig.

202   3). In contrast, successful trial classification pertaining to lexical decisions was driven by neural

203   activity increases in the left anterior subregion and neural activity decreases in the right anterior

204   subregion, relative to the other two tasks. Finally, neural activity within both posterior subregions

205   carried salient information that was instrumental in successfully discriminating trial brain scans

206   recorded during perspective taking.

207   **Task-specific network connectivity resembles task complexity**

208   We subsequently delineated the task-dependent profiles of how IPL subregions are functionally

209   coupled with regions outside the IPL ROI. For this purpose, we assessed functional connectivity

210   between the four IPL subregions and other cortical brain regions. By means of non-parametric

211   permutation testing, we tested for statistically significant coupling differences (Fig. 4 and Fig. S4).

212   The connectivity profiles between the four IPL subregions and large-scale brain networks were

213   significantly different between tasks. The anterior subregions showed strong degrees of hemispheric

214   lateralization and domain specificity. In contrast, the posterior subregions showed less lateralization

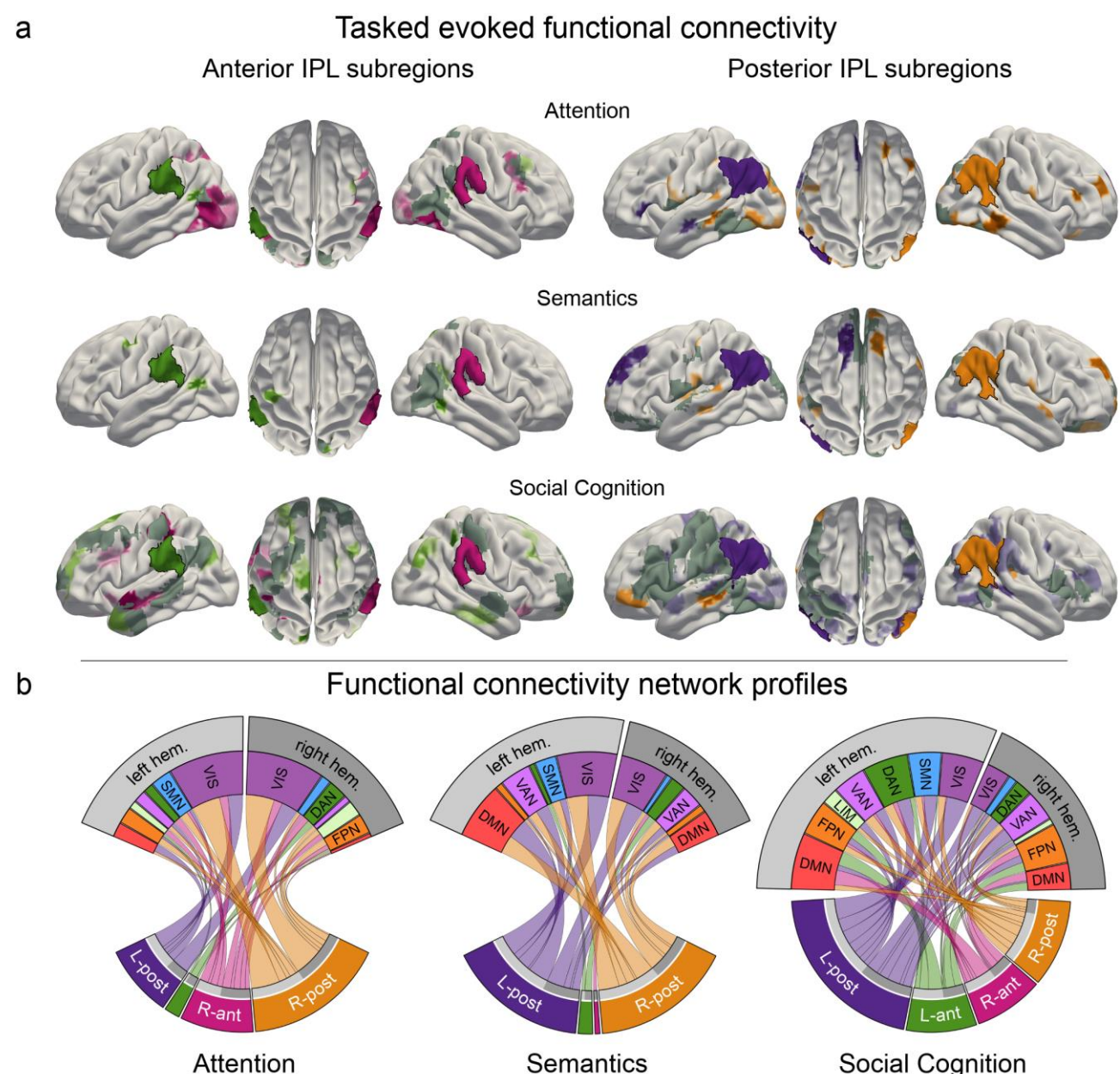215   and a higher degree of across-network coupling.

11

Fig. 4. Task-induced shifts in cortex-wide functional connectivity. Task-dependent functional connectivity profiles of the four IPL subregions with other coupling partners, compared to the respective other tasks. **(a)** Task-specific correlation between anterior (left) and posterior (right) IPL subregions and brain-wide cortical regions. All results are statistically significant at $p < 0.05$, tested against the null hypothesis of indistinguishable connectivity strength between a given IPL subregion and the rest of the brain across all three tasks. L-ant: left anterior IPL subregion; L-post: left posterior IPL subregion; R-ant: right anterior IPL subregion; R-post: right posterior IPL subregion. Dark gray: mutual connectivity target. **(b)** Task-specific connectivity profiles of the four IPL subregions with seven large-scale brain networks (Yeo et al., 2011). DAN: dorsal attention network. DMN: default mode network. FPN: fronto-parietal network. LIM: limbic network. VAN: ventral attention network. SMN: somatomotor network. VIS: visual network.

Subregion-specific functional connectivity: Figure 4–figure supplement 1

12

228   *Task-specific connectivity profiles for anterior IPL subregions*

229   During attentional reorienting, the right anterior IPL subregion was stronger involved in cortex-wide

230   connectivity than its left-hemispheric counterpart (Fig. 5A, left column; Fig. 5D). The visual network

231   and regions belonging to the dorsal attention network emerged as its preferred coupling partners (Fig.

232   S4). The left anterior subregion was less engaged in cortical connectivity, and showed the strongest

233   coupling with the dorsal attention network and the fronto-parietal control network. Compared to the

234   other two functional domains, lexical decisions led to less cortex-wide connectivity, most strongly

235   with left hemispheric dorsal attention network regions. In contrast, the perspective taking connectivity

236   profiles for the left and right anterior subregions showed coupling with various networks. These IPL

237   subregions revealed the strongest coupling patterns with left-hemispheric default mode network and

238   bilateral fronto-parietal control network regions.

239   *Task-specific connectivity profiles for posterior IPL subregions*

240   During attentional reorienting, specific cortical connectivity shifts emerged for the right posterior

241   subregion rather than the left posterior subregion of the IPL ROI (Fig. 5A, right column; Fig. 5D).

242   Relative to the other two tasks, attentional reorienting led to significantly enhanced functional

243   coupling with the visual network and left-hemispheric parts of the somatomotor network, as well as

244   increased connectivity with right-hemispheric parts of the fronto-parietal control network (Fig. S4).

245   Processing lexical decisions in turn was specifically characterized by coherent connectivity increases

246   between the posterior IPL subregions and the bilateral visual network, the default mode network and

247   the ventral attention network. Finally, engagement in perspective taking engendered significantly

248   stronger functional connectivity for the left posterior subregion and extended parts of several large-

249   scale brain networks. While the left posterior subregion showed similar connectivity strength to

250   bilateral parts of large-scale networks, the right posterior subregion mainly interacted with

251   contralateral parts. The posterior IPL regions showed connectivity links with multiple coupling

252   partners, including regions belonging to the visual network, to the ventral and dorsal attention

253   network, and to the somatomotor network.

13

254 **Causal interactions between IPL subregions are task-dependent**

255 To complement our findings on the task-evoked shifts in broader cortical connectivity profiles, we

256 used dynamic causal modeling (DCM) to identify directed task-specific connectivity modulations

257 between IPL subregions. The DCM optimization procedure provided one Bayesian parameter average

258 group-level model. All modulatory parameters of this optimal model exceeded zero given a 95%

259 confidence interval. Permutation-based tests provided evidence for task-specific differences in the

260 emerging modulatory configurations among the IPL subregions (Fig. 5, see Table 2 for modulatory

261 parameter estimates between subregions and Table S2 for other model parameters).
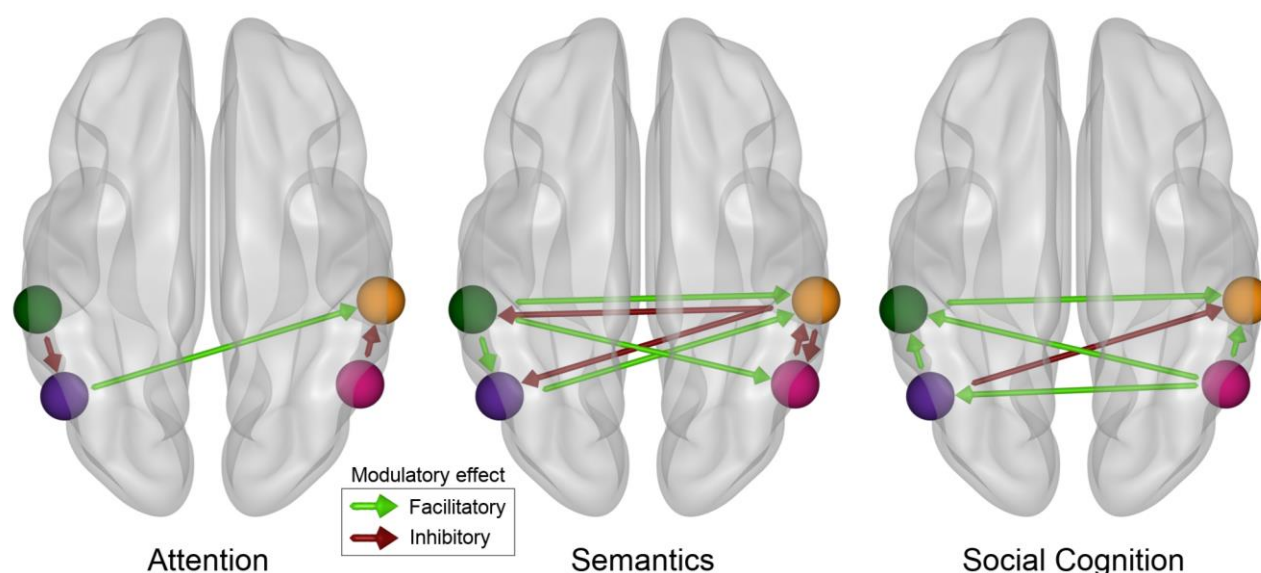

263 **Fig. 5. Tasks cause different effective connectivity modulations among IPL subregions.** The modulation

264 assessed by dynamic causal modeling (DCM) of directed connectivity among the four IPL subregions differs

265 between attentional reorienting, lexical decisions, and perspective taking. Only significant modulatory

266 parameters ($\alpha \leq 0.01$) are shown (based on the non-parametric permutation analysis). Attentional reorienting

267 induces comparatively simple connectivity modulations, while both other tasks are characterized by richer

268 changes in the modulatory influences between subregions. Lexical decisions increase facilitatory influences

269 from the left to the right hemisphere and inhibition from the right to the left. Perspective taking causes bilateral

270 increases in the facilitatory influence from posterior to anterior subregions. Green: DCM node in the left

271 anterior subregion (L-ant). Violet: DCM node in the left posterior subregion (L-post). Orange: DCM node in

272 the right anterior subregion (R-ant). Pink: DCM node in the right posterior (R-post) subregion.

14

273   Explicitly probing modulatory effects on directed connectivity within the IPL, attentional

274   reorienting was characterized by a simple coupling configuration, with three significant modulations:

275   An increased inhibitory influence from the left anterior to the left posterior subregion, a facilitatory

276   drive from the left posterior to the right anterior subregion, and an inhibitory influence from the right

277   posterior to the right anterior subregion (Fig. 5, left). The attention coupling topology was

278   distinctively closer to the intrinsic connectivity than effective modulation patterns underlying both

279   other domains. Both other tasks prompted more complex patterns of coupling modulations among

280   IPL subregions. During lexical decisions, we found strong interhemispheric modulations, both

281   facilitatory and inhibitory, between IPL subregions. Strikingly, task-related connectivity increases

282   from the left anterior subregion to all other subregions were facilitatory. In contrast, the right anterior

283   subregion had an inhibitory influence on all other subregions (Fig. 5, center). Perspective taking was

284   mainly characterized by increased facilitatory influences between IPL subregions, with the right

285   posterior subregion exerting a facilitatory influence on all other subregions (Fig. 5, right panel).

286   Interhemispheric interactions between subregions were also mainly facilitatory during perspective

287   taking (Fig. 5, left).

288   To summarize, the three cognitive domains of interest were characterized by fundamentally

289   different motifs of effective connectivity modulations among IPL subregions. A core observation

290   relies on a simple directed connectivity profile for attentional reorienting and more complex directed

291   connectivity interactions between IPL subregions for both higher-level tasks.

292   **Table 2. Task-specific effective connectivity modulation**

Source subregion		Target subregion	Modulation strength	p-value
Attention				
L-ant	→	R-post	-1.93	0.0017
L-post	→	R-ant	3.01	0.0033
R-post	→	R-ant	-1.50	0.0007
Semantic				
L-ant	→	L-post	1.08	0.0012
L-ant	→	R-ant	0.97	<0.0001

L-ant	→	R-post	1.27	0.0026
L-post	→	R-ant	1.26	<0.0001
R-ant	→	L-ant	-1.49	0.0031
R-ant	→	L-post	-2.45	0.0001
R-ant	→	R-post	-3.24	<0.0001
R-post	→	R-ant	-0.22	<0.0001
Social Cognition				
L-ant	→	R-ant	0.30	0.0078
L-post	→	L-ant	1.23	<0.0001
L-post	→	R-ant	-0.57	0.0013
R-post	→	L-ant	1.76	<0.0001
R-post	→	L-post	1.43	<0.0001
R-post	→	R-ant	2.13	<0.0001

293 *Note:* Significant modulatory parameters ('B-matrix', $\alpha \leq 0.01$) of connectivity between subregions.

294 Based on a random effects permutation test for the null hypothesis 'no parameter difference between

295 tasks'. The strength is given as posterior expectation from the optimum Bayesian parameter average

296 model.

Discussion

298 The inferior parietal lobe is a foremost convergence zone of diverse mental capacities, several of

299 which are potentially most developed in the human species. However, it remains open to question

300 how some of the most basic and some of the most advanced cognitive processes converge and diverge

301 in the IPL to realize human communication and interaction. To address this unresolved issue from

302 different perspectives, we carried out a multi-method investigation that makes the functional

303 specialization within the IPL apparent across attention, semantics, and social cognition tasks. By

304 pooling insight from predictive, causal, and functional coupling analyses, we revealed a functional

305 triple dissociation between the probed cognitive domains in the IPL at subregion-resolution. Based

306 on neural activity estimates for the three domains, two distinctable subregions, one anterior and one

307 posterior, were identified per IPL by a functional parcellation analysis. These subregions differed in

308 their functional specialization across hemispheres and cognitive functions. The right anterior IPL

16

309   subregion showed the strongest predictive relevance for attentional reorienting while the left anterior

310   IPL subregion was strongest associated with semantic processing. In contrast, both left and right

311   posterior IPL were robustly engaged when subjects adopted the mental perspectives of others.

312   Functional specialization within the larger IPL regions also differed with respect to whole brain

313   connectivity profiles for the different subregions. In general, we observed increased connectivity with

314   diverse large-scale networks with increasing cognitive complexity across tasks. Global connectivity

315   profiles for the anterior IPL subregions showed strong hemispheric lateralization and domain

316   specificity. Functional connectivity profiles for the left and right posterior subregions were similar

317   within each task and showed a higher degree of across-network coupling. Complementary effective

318   connectivity profiles between specialized IPL subregions also differed across domains, supporting

319   the notion of stronger coupling with increasing cognitive complexity. The degree of functional

320   specialization of the IPL has been contemplated before (Seghier, 2013). Yet, only in recent years,

321   direct comparison of task experiments from different cognitive neuroscience domains, conventionally

322   studied in isolation, has enjoyed increasing attention (Bzdok et al., 2013, 2016; Igelström et al., 2016).

323   Our present study invigorates these beginning endeavors to transcend cognitive fields that are

324   typically studied independently by separate research communities. We strive towards such cross-

325   pollination across disparate literature streams.

326   To pursue this goal, we show that domain-specific functional signatures became apparent

327   within the IPL when interrogating neural activity responses to tasks, derived predictive principles, as

328   well as modulations of directed connectivity among IPL subregions and their functional coupling

329   profiles with distributed brain regions. It is a key advantage that our findings were based on carefully

330   controlled experimental paradigms that were administered to the same subject sample. Consequently,

331   our study offers critical new elements of synthesis that pave the way for a more holistic perspective

332   of IPL specialization.

333   First, the right IPL showed strong engagement in attentional processes in our study. Previous

334   work has demonstrated a causal relation between tissue damage to the right IPL and left spatial neglect

17

335   (Thiebaut de Schotten et al., 2014). Such neurological patients routinely fail to process cues in their

336   contralesional visual field. Additionally, transient virtual lesions of the right, but not left IPL in the

337   intact human brain were reported to cause performance declines during attentional reorienting

338   (Rushworth et al., 2001). Our findings corroborate and detail this previous research by carefully

339   locating attentional processing and accompanying functional coupling shifts preferentially in the

340   anterior subregion of the right IPL, compared to semantics and social cognition. Moreover, neural

341   activity in the right anterior IPL subregion contained information that enabled successfully

342   discriminating attentional reorienting from semantics and social cognition in our predictive modeling

343   analyses. The new insights on right-hemispheric lateralization of attentional reorienting in the IPL

344   were further refined by unique and simple effective connectivity modulations between IPL

345   subregions. Additionally, our analyses of global functional coupling patterns revealed that the right

346   anterior IPL subregion stands out by its connections to bilateral fronto-parietal and visual-sensory

347   networks. Together, these findings speak to a specialized neuronal infrastructure harbored within the

348   right anterior IPL, which is especially tuned to processing demands of attentional reorienting.

349   Second, our results isolate strong engagement of the anterior subregion of the left IPL for

350   semantic processing. Deficits in various facets of semantic processes, such as in Wernicke's aphasia

351   (Corbetta et al., 2015), have received evidence to be closely linked to left temporo-parietal damage

352   (Corbetta et al., 2015; Dronkers et al., 2004; J. Fridriksson et al., 2016; Julius Fridriksson et al., 2010;

353   Mirman & Graziano, 2012; Schwartz et al., 2011) among other regions of the language network.

354   Consistently, transient virtual lesions of the left IPL in healthy subjects were reported to disrupt

355   semantic task performance during language comprehension (Hartwigsen et al., 2017; Sliwinska et al.,

356   2015). Our findings from mapping neural responses during experimental tasks and identifying most

357   predictive subregions reliably situated semantic processing in the left anterior IPL subregion. In

358   addition, our effective connectivity analyses revealed a motif of rich modulatory influences among

359   IPL subregions during semantic processing compared to our other two tasks. Specifically, we found

360   increased task-induced facilitatory coupling from the left to the right IPL, with the left anterior IPL

18

361   increasing its facilitatory influence on all other subregions during semantic processing. The strong

362   facilitatory modulation exerted from the left to the right IPL was complemented by increased

363   inhibition in the influence of the right on the left IPL and between right-hemispheric IPL subregions,

364   potentially reflecting cognitive control processes (e.g. inhibition of alternative responses). This

365   constellation of task-induced connectivity modulations is consistent with an interpretation of fine-

366   grained interactions between left and right IPL subregions, rather than an exclusive role of the

367   dominant left hemisphere in language processing (see also Binder et al., 2009; Hartwigsen, 2018;

368   Hartwigsen et al., 2020).

369   Third, adding to the right and left anterior IPL's preferential involvement in attentional and

370   semantic processing, respectively, our perspective taking task highlighted the posterior subregion of

371   the IPL in both hemispheres as key regions for social cognition. This last piece of the functional triple

372   dissociation in the IPL received support from our multivariate predictive algorithm approach, and

373   was further annotated by our effective connectivity analyses. When subjects were concerned with

374   inferring others' mental states, both posterior IPL subregions increased their facilitatory influence on

375   the bilateral anterior IPL subregions. The overall task-specific connectivity configuration derived for

376   our social cognition task was predominantly facilitatory, pointing towards tight intra- and

377   interhemispheric interactions during mental perspective taking. A posterior-to-anterior transition of

378   the neurocognitive processes subserved by the IPL has been proposed in previous research (Bzdok et

379   al., 2016; Gordon et al., 2020). These authors identified the posterior IPL as relatively higher

380   associative and more domain-general processing hub, compared to the anterior IPL subregions. More

381   broadly, the observed bilateral IPL engagement in widely employed social cognition experiments

382   carefully reconciles previous virtual lesion evidence on the functional relevance of the overall right

383   (Krall et al., 2016) or left (Samson et al., 2004) IPL region for social cognitive functions.

384   Our compilation of findings provides a multi-perspective answer to the functional

385   subspecialization of the IPL that spans lower and higher cognitive processes. Previous studies have

386   hinted at or considered the possibility of several specialized subregions in the IPL (Bzdok et al., 2013,

387   2016; Kernbach et al., 2018). While some authors have advocated a monolithic functional role of the

388   IPL, others advertised the possibility of functionally distinct neuronal populations in the IPL, which

389   may be challenging to disentangle using conventional contrast analysis in neuroimaging. To the best

390   of our knowledge, we are the first to conduct a within-subject study across such a diversity of

391   cognitive domains. Thereby, we demonstrate that cognitive processing in the IPL can probably not

392   be accounted for by a single account of functional specialization.

393   Based on our examination of three functional domains with different experimental tasks, two

394   robust clusters of neural responses within the IPL were identified, each of which probably overlaps

395   with several cytoarchitectonic areas. The observed functional differentiation along the anterior and

396   posterior IPL region is consistent with previous work in human volunteers, which featured such

397   functional gradients based on resting-state connectivity (Mars et al., 2011), meta-analytic

398   connectivity modeling (Bzdok et al., 2016), and probabilistic fiber tracking (Caspers et al., 2011).

399   More anterior portions of the IPL in the left hemisphere were reported to be more specifically

400   associated with lower-level neural processing facets of language and social cognition. Instead, more

401   posterior portions of the IPL were more specifically associated with advanced neural processing

402   facets of both functional domains (Bzdok et al., 2016). This observation converges with the present

403   constellation of findings. The relatively automatic lexical decision task in the present study was

404   specifically associated with our left anterior IPL cluster, while the more complex perspective taking

405   task was specifically associated with both posterior IPL subregions. Consistently, our functional

406   connectivity analysis demonstrated relatively stronger across-network coupling with several cortical

407   networks for our posterior IPL cluster.

408   A functional dissociation in the specialization of anterior and posterior IPL regions is further

409   consistent with findings in non-human primates (Rozzi et al., 2008). Anterior parts of the monkey

410   IPL are functionally specialized in somatosensory processes, whereas posterior parts preferentially

411   process information based on visual input (Kravitz et al., 2011). The posterior part is thought to be

412   particularly involved in navigation, that is, processing one's position in space (Crowe et al., 2004,

20

413 2005). This region is further associated with processing visual information in an external, object-

414 centered manner (Crowe et al., 2008) compared to an egocentric processing system which is used to

415 control body movements (Chafee et al., 2007; Snyder et al., 1998). These findings argue for increased

416 processing complexity from anterior to posterior regions in the macaque IPL. It is however important

417 to bear in mind that the monkey-human homologue of IPL anatomy remains insufficiently understood

418 (Mars et al., 2013; Seghier, 2013).

419   A high degree of abstraction from sensory information in the macaque IPL is further

420 substantiated by the existence of intention- and goal-specific neurons rather than pure movement-

421 coding neurons in the macaque IPL (Fogassi et al., 2005; Rozzi et al., 2008). Notably, the IPL

422 expanded in the primate lineage (Orban et al., 2004), while the existence of a homologue in non-

423 human primate remains uncertain (Mars et al., 2011; Seghier, 2013). The expansion of the IPL may

424 relate to cognitive capacities which are unique to humans, including the ability for speech and

425 language processing as well as complex problem solving. We confirm and detail the previously

426 reported gradient in the complexity of processing in the human IPL, which likely reflects fine-tuned

427 functional differentiation for higher cognitive operations in humans.

428   Distinct functional specialization for human-defining cognitive operations in the IPL may

429 explain differences in the connectivity profiles of the larger IPL regions between humans and

430 macaques (e.g. Margulies et al., 2016; Oligschläger et al., 2018; Xu et al., 2020). Uncertain

431 homologies between humans and non-human primates are accompanied by complex structure-

432 function relationships in the human IPL. As an overarching tendency, functional organization

433 reproduces structural organization in unimodal areas in the human brain. In contrast, functional

434 organization is significantly less determined by structure in heteromodal brain regions (Vázquez-

435 Rodríguez et al., 2019). Such laxer coupling of structure-function relations is observed in heteromodal

436 association areas, including the IPL (Margulies et al., 2016). In general, functional specialization for

437 higher cognitive operations may gradually decouple from the underlying structure (Vázquez-

21

438   Rodríguez et al., 2019). This notion is in line with the present results from our functional parcellation

439   which does not simply follow cytoarchitectonic boundaries.

440   Our complementary set of findings indicate that task-specific effective connectivity

441   modulations within and from different IPL subregions uniquely characterize each of the probed

442   cognitive domains. For relatively low-level cognitive processes, here exemplified by attentional

443   reorienting, task-specific coupling adjustment implicated a reduced set of coupling partners. In

444   contrast, for more complex tasks, as exemplified by lexical decision and perspective taking, we found

445   evidence for more elaborate coupling motifs, including dense intra- and inter-hemispheric facilitation

446   and inhibition. Notably, there is a scarcity of existing studies directly devoted to investigating the left

447   and right IPL in several different psychological tasks. The few existing studies committed to the

448   effective connectivity of the IPL mainly focused on task-related connectivity changes between an IPL

449   subregion and other areas of a specialized network for a single cognitive domain, typically in one

450   hemisphere only (Fukuda et al., 2019; Hartwigsen et al., 2017). As such, our results usher towards a

451   broader perspective. We complement the identification of intra- and inter-hemispheric IPL coupling

452   patterns with strong domain-specific coupling profiles from IPL subregions to disparate cortical

453   partners from large-scale brain networks.

454   Task-induced shifts in functional connectivity revealed key distinctions in interactions with

455   major brain networks. Functional coupling profiles varied significantly between the three

456   experimental tasks. Across domains, coupling partners were recruited from various large-scale brain

457   networks. Our observation reinforces the notion of the IPL interfacing multiple neural systems and

458   different levels of neurocognitive abstraction (Bzdok et al., 2013; Seghier, 2013).

459   Moreover, we show that the task-specific coupling profiles between IPL subregions and a

460   variety of cortical partners are anchored in the functional compartments uncovered in the IPL. The

461   wider functional connectivity profiles for the anterior and posterior subregions further elucidate their

462   features of underlying neural processing. As a tendency, functional connectivity profiles for the left

463   and right posterior subregions were similar within each task. Yet, global connectivity profiles varied

464   between the left and right anterior subregions of the IPL. The hemisphere-specific functional coupling

465   for the anterior IPL subregions is broadly consistent with the common reports of right-hemispheric

466   specialization of attentional reorienting processes (Rushworth et al., 2001; Schuwerk et al., 2017) and

467   left-hemispheric specialization for semantic processes (Binder et al., 2009; Braga et al., 2019;

468   Hartwigsen et al., 2016). The rich connectivity profiles of the left and right posterior IPL subregions

469   support the notion of bilateral IPL relevance for social cognitive processes, consolidating previous

470   findings (Bzdok et al., 2013, 2016).

471   Specifically, during attentional processing, the dedicated coupling partners of the right

472   anterior IPL subregion included regions of the visual cortex and the dorsal attention network. During

473   semantic processing, the left anterior subregion enhanced coupling with regions of the default mode

474   and ventral attention network. Ultimately, during social cognition processing, the left and right

475   posterior IPL subregions preferably coupled with the default mode network. The observed task-

476   specific functional coupling of the posterior subregions with major brain networks was largely

477   symmetric across both hemispheres.

478   To summarize our integrated experimental and computational study, we provide evidence for

479   a functional triple dissociation in the human IPL, with task-specific functional specialization in

480   distinct IPL subregions. This emerging view is supported by information carried in precise

481   multivariate predictive signatures. Zooming into task-specific coupling motifs among IPL subregions,

482   our effective connectivity analyses revealed that attentional reorienting mediated simpler coupling

483   modulations, while semantic and social cognition were realized by more complex inter-hemispheric

484   influences. Delineating task-evoked shifts in functional coupling patterns, in turn, uncovered that the

485   posterior IPL subregions were linked to bilateral, symmetric recruitment of distributed cortical

486   coupling partners, reminiscent of the default mode network. Conversely, the anterior IPL subregions

487   were engaged in flexible and hemisphere-specific coupling patterns with brain-wide cortical partners.

488   Together, our results shed new light on how currently under-appreciated activity and connectivity

489   profiles within the left and right IPL support some of the most distinctive mental capacities in humans.

Materials and Methods

Subject sample

Twenty-two healthy, native German speakers (11 female, mean age 27.9 ±3.28 years) participated in this neuroimaging investigation. All subjects had normal or corrected-to-normal vision and no contraindications against magnetic resonance imaging (MRI). Subjects were recruited from the inhouse database at the Max Planck Institute for Human Cognitive and Brain Sciences. Written informed consent was obtained from all subjects before the experiment. All subjects were right-handed (laterality index ≥80% (Oldfield, 1971)). The study was performed according to the guidelines of the Declaration of Helsinki and approved by the Ethics Committee of the Medical Faculty of the University of Leipzig, Germany.

Experimental design

The functional MRI (fMRI) investigation (see Fig. S1A) consisted of three sessions that were performed on separate days, scheduled at least seven days apart from each other. Each fMRI session was divided into four runs. In all runs, each of the three tasks (i.e., attentional reorienting, lexical decisions, and perspective taking, see below for details) was administered consecutively in a task block. Within task blocks, trials were presented in an event-related fashion. Each run consisted of 40 attentional reorienting trials (8 *invalid*, 30 *valid*, 2 *catch* trials), 40 lexical decision trials (20 *word* and 20 *pseudoword* trials), and 6 perspective taking trials (3 *false belief* and 3 *true belief* trials). Each stimulus for the lexical decision and social cognition task was only shown once per subject, while the attentional reorienting task relied on simple geometric cues that were presented repeatedly. At the beginning of each task block, instructions were presented. Task order was pseudo-randomized. Trial order and timing were defined by a genetic algorithm for optimizing detection power, using an adapted version of Neurodesign v0.2.1 (Durnez et al., 2018). All experimental tasks were administered with Presentation Software (v20.1; Neurobehavioral Systems, Berkeley, CA). Prior to the first fMRI session, subjects underwent training for all three tasks outside the MRI scanner.

515   Training stimuli for the semantic and the social cognition task were not included in the main

516   experiment.

Tasks

518   For each probed cognitive domain, we elected a well-established task. Task presentation and response

519   selection were carefully matched across tasks, including visual stimuli and binary choices for all

520   tasks. All three tasks conformed to the principle of using a single target condition and a single control

521   condition to isolate the neural activity of the particular cognitive function. In all three tasks the

522   subjects responded to a binary choice after each trial via single button press on a two-finger response

523   box with their right hand. Button assignments for the semantic and social cognition tasks were

524   initially pseudo-randomized across subjects, and kept identical across sessions per subject. The button

525   box was fixated on the subject's right thigh to assure a comfortable, natural, and stable lying position

526   in the MR scanner. Subjects were instructed to respond as fast and accurately as possible. Example

527   trials for each of the different tasks and conditions are available in Fig. S1.

Attention

529   We used a Posner-like attentional reorienting task, as described previously (Rushworth et al., 2001).

530   Each trial started with the presentation of two rectangular, empty boxes (size 2.6° of visual angle,

531   center distance 8.3°, positioned horizontally) and a fixation cross at the center of the screen (Fig.

532   S1B). After an average duration of 3.2 s (SD = 1.41 s, minimum interstimulus interval = 2 s), the

533   fixation cross was replaced with an arrow pointing either to the right or the left for 250 ms or 350 ms

534   (the 'cue'). Subsequently, a target asterisk was presented in one of the rectangles. In 75% of the trials,

535   the target location was congruent with the direction of the arrow (*valid* condition). In 20% of the

536   trials, the target was presented on the (unexpected) opposite side (*invalid* condition). In 5% of the

537   trials, no asterisk was shown (*catch* condition) and no response was probed to ensure constant

538   attention. Subjects were asked to indicate the location of the target with a button press. Note that the

539   *invalid* condition was intended to recruit attentional reorienting processes. Instead, the *valid* condition

540   served as the matched control condition.

25

541 *Semantics*

542 We administered a lexical decision task that contrasts words and pseudowords as a prototypical

543 example of semantic processing (Binder et al., 2003). 240 concrete German nouns were selected from

544 the SUBTLEX-DE database (Brysbaert et al., 2011). Inclusion criteria were i) two syllables; ii)

545 frequency per million > 1; iii) concreteness ratings < 4; and iv) arousal ratings < 6, according to the

546 LANG rating (note that smaller values correspond to a higher concreteness (Kanske & Kotz, 2011)).

547 All word stimuli denoted countable entities and were non-ambiguous. A pseudoword was created for

548 each word with Wuggy v0.2.2b2 (Keuleers & Brysbaert, 2010) to assure phonotactic validity without

549 semantic content. Pseudowords matched their word counterparts in length, syllable structure, and

550 transition frequencies between subsyllabic elements. Each trial started with the presentation of a

551 fixation cross for at least 2 s (M = 3.8 s, SD = 1.7). Thereafter, a *word* (target condition) or

552 *pseudoword* (control condition) was shown for 1 s. Subjects were instructed to indicate whether the

553 stimulus represented a word or pseudoword via button press (Fig. S1C).

554 *Social cognition*

555 For the perspective taking task, we employed an adapted version of the Sally-Anne paradigm, which

556 is known to prompt reasoning about the mental state of others (Rothmayr et al., 2011). In total, 72

557 three-picture comics were presented, with 2 s presentation time per stimulus. Between trials, a

558 fixation cross was shown for at least 2 s (M = 3.8 s, SD = 1.7 s). In all trials, character A puts an

559 object into a container-like object (picture 1). Then character B passes the object on to another

560 container. Character A either observes this action (*true belief*) or not (*false belief*) (picture 2) and then

561 searches in either the correct or in the wrong location (picture 3). Subjects were instructed to indicate

562 whether the search location was congruent or incongruent with character A's knowledge about the

563 object position via button press (Fig. S1D). A correct response during a *false belief* trial (target

564 condition) required the subject to infer the mental state of character A from the comic narrative. In

565 contrast, for the control condition (*true belief*) a correct response did not depend on perspective taking

566 and could be accomplished by relying on the physical reality shown to the subjects.

Functional magnetic resonance imaging

fMRI data acquisition was performed on a 3 Tesla Siemens Prisma system (Siemens, Erlangen, Germany). A whole brain gradient echo planar (GE-EPI) T2* sensitive sequence (3x3x3.2 mm, 0.32 mm gap, TR 0.5 s, 36 slices, TE 24 ms, flip angle 45°) with multiband acceleration was used (Feinberg et al., 2010). Additionally, a high-resolution (1x1x1 mm voxel size) structural MR image (T1w) was acquired for each subject using a standard three-dimensional MPRAGE sequence.

Preprocessing

The raw fMRI data was despiked with 3dDespike from the AFNI toolbox through Nipype v1.5.0 (Gorgolewski et al., 2011). Subsequently, the preprocessing was implemented in fMRIPrep v1.4.1 (Esteban et al., 2019), a Nipype based tool. The individual T1 image was intensity corrected using N4BiasFieldCorrection v2.1.0 (Tustison et al., 2010) and skull-stripped using antsBrainExtraction.sh v2.1.0 with the OASIS (Marcus et al., 2007) template. Brain surfaces were reconstructed using recon-all from FreeSurfer v6.0.1 (Dale et al., 1999). A brain mask was refined to reconcile ANTs-derived and FreeSurfer-derived segmentations of the cortical gray matter in Mindboggle (Klein et al., 2017). Spatial normalization to the ICBM 152 nonlinear asymmetrical template version 2009c (Fonov et al., 2009) was performed through nonlinear registration with the antsRegistration tool 2.1.0 (Avants et al., 2008). Brain tissue segmentation of cerebrospinal fluid, white matter and gray matter was performed on the brain-extracted T1 with the fast tool (FSL v5.0.9 (Zhang et al., 2001)).

Functional data was slice-time corrected with 3dTshift from AFNI v16.2.07 (Cox, 1996) and motion corrected using mcflirt (FSL v5.0.9 (Jenkinson et al., 2002)). Distortion correction was performed with the TOPUP technique (Andersson et al., 2003) using 3dQwarp from the AFNI toolbox. This was followed by co-registration to the T1 using boundary-based registration (bbregister from FSL v6.0.1 (Greve & Fischl, 2009)) with nine degrees of freedom. Motion correction transformations, field distortion correcting warp, functional-to-anatomical transformation and T1-to-

591 MNI warp were concatenated and applied in a single step using antsApplyTransforms (ANTs v2.1.0)

592 with Lanczos interpolation.

593   To account for motion induced artefacts, physiological noise regressors were extracted with

594 the anatomical version of CompCor (Behzadi et al., 2007) (aCompCor). Six components were

595 calculated within the intersection of the subcortical mask and the union of corticospinal fluid and

596 white matter masks. Frame-wise displacement (Power et al., 2014) was calculated using the

597 implementation of Nipype.

598 Statistical Parametric Mapping 12 (SPM 12, Wellcome Department of Imaging Neuroscience,

599 London, UK) was used to spatially smooth the functional data with an 8 mm full-width half-maximum

600 Gaussian kernel.

601 **Specification of the general linear models**

602 At the single-subject level, two design matrices were specified and general linear models (GLMs)

603 were computed using SPM 12 (Wellcome Department of Imaging Neuroscience, London, UK) to

604 estimate task-related neural activity. GLM_{cond} was designed with one regressor per condition in

605 accordance with the standard mass-univariate analysis. The second set of GLMs (GLM_{trial}) was

606 purpose-designed for multivariate and task-related functional connectivity analyses with one

607 regressor per trial to gain access to trial-wise neural activity estimates (Abdulrahman & Henson,

608 2016). For GLM_{cond}, seven trial regressors were defined (*valid*, *invalid*, *catch*, *word*, *pseudoword*,

609 *false belief*, *true belief*, duration 0 s). Additionally, three rest regressors for task-wise rest periods

610 were included (duration 16 s each). Incorrect responses were modelled separately per task. One

611 regressor per session was added to account for between session variability. To remove high-motion

612 timepoints, one volume masking regressor was added for each volume with a frame-wise

613 displacement value above 0.9 (Power et al., 2012), yielding an average of 10.04 masked volumes per

614 subject. Six motion and six aCompCor (Behzadi et al., 2007) regressors were included to account for

615 motion-induced artefacts. The design matrix for GLM_{trial} followed a similar general logic, but

616 included one regressor per trial, leading to trial wise-beta estimates instead of condition-wise beta

617 estimates. Run, motion, and aCompCor regressors were added as above. GLM_{cond} was estimated on

618 smoothed, GLM_{trial} on unsmoothed data. A high-pass filter of 128 s was applied and serial

619 correlations were accounted for with the FAST method (Corbin et al., 2018). Global normalization

620 was not performed and the canonical hemodynamic response function was used without derivatives.

Classical statistical analysis

622 For each task, two contrasts were defined at the single-subject level, including the condition of interest

623 $>$ rest$_{task}$ (*invalid* $>$ rest$_{att}$, *word* $>$ rest$_{sem}$, & *false belief* $>$ rest$_{soc}$) and control condition $>$ rest$_{task}$ (*valid*

624 $>$ rest$_{att}$, *pseudoword* $>$ rest$_{sem}$, *true belief* $>$ rest$_{soc}$). Task-wise contrasts (*invalid* $>$ *valid*, *word* $>$

625 *pseudoword*, *false belief* $>$ *true belief*) were computed at the group level.

626 Brain results were rendered by means of Paraview v5.7.0 (Ahrens et al., 2005), circlelize v0.4.8 (Gu

627 et al., 2014), and BrainNet Viewer v1.7 (Xia et al., 2013). To this end, results were transformed from

628 MNI space (ICBM 152 linear (Mazziotta et al., 2001)) to the surface-based FreeSurfer fsaverage

629 (Fischl et al., 1999) coordinate system via the nonlinear mapping Registration Fusion approach v0.6.5

630 (Wu et al., 2018).

Subregion identification in the IPL

632 The topographical outline for the left and right IPL ROI was guided by an established and freely

633 available histological atlas. Seven cytoarchitectonic maps cover the human IPL in each hemisphere

634 according to the widely used JuBrain probabilistic cytoarchitectonic atlas (Amunts & Zilles, 2001).

635 These anatomical definitions of microstructurally defined areas known to exist in the IPL comprised

636 one rostral (PGp) and one caudal (PGa) region in the angular gyrus, and five regions of the

637 supramarginal gyrus (PFm, PF, PFop, PGcm, PFt), as provided by the SPM 12 Anatomy Toolbox

638 v2.2b (Eickhoff et al., 2005). The outer boundary of the conglomerate of these cytoarchitectonic areas

639 was taken as contours of our ROI in the IPL, separately in the left and right hemisphere. Both of our

29

640   ensuing ROI definitions occupied similar cortical volume: 1102 voxels in the left and 1123 voxels in

641   the right (Fig. 2A) hemisphere.

642   We used tools from machine learning to explore coherent solutions to IPL segregation in the

643   context of our experimental tasks. A k-means clustering (Hartigan & Wong, 1979) was applied at the

644   voxel level with 1,000 random centroid initializations (Thirion et al., 2014) based on the estimates

645   from the "target condition > rest" contrast of the GLM_{cond} in the IPL ROIs. The unsupervised

646   clustering algorithm was applied on pooled information across subjects and separately for each

647   hemisphere. To explore an optimal number of clusters, hemisphere by hemisphere, our choice was

648   anchored in the majority vote taken across 25 distinct cluster validity metrics that were computed for

649   candidate solutions with 2 to 7 clusters using NBClust v3.0 (Charrad et al., 2014). Each cluster quality

650   metric provided a ranking of candidate cluster numbers based on a different notion of goodness-of-

651   fit of the candidate solutions. The majority vote of these different ranking criteria provided a

652   principled, data-driven rationale for the final cluster number that we endorsed in our study, in each

653   hemisphere. To ensure robust voxel-to-cluster assignments, all solutions from the 1,000 algorithms

654   initializations that resulted in the winning cluster number were merged into one final solution.

655   Specifically, the final assignments of voxel-to-cluster responsibilities were based on agreement across

656   the random algorithm initializations. Voxels with varying cluster allocations across the initializations

657   were excluded from the final cluster solution (cf. Results section).

658   **Task-predictive information of the IPL subregions**

659   After establishing functionally defined subregions in our IPL ROIs, we directed attention to the

660   information content available at subregion granularity. For this purpose, we carried out a one-versus-

661   rest scheme in combination with a sigmoid-loss (logistic) linear predictive algorithm to automatically

662   detect the task membership of single experimental trials directly from subregion-wise averaged neural

663   activity signals. Model parameter estimation and model evaluation of predictive success were

664   performed conjointly for the three target conditions (*invalid*, *word*, *false belief*). This modeling

665   strategy naturally yielded a set of predictive weights for all subregions for each task. Appropriately

666   balanced numbers of trials were ensured for all conditions by sub-sampling to the minimum number

667   of trials per subject and fMRI run. We exclusively considered task trials and brain scans with correct

668   responses. Signal deconfounding removed variation that could be explained by session number,

669   session time, subject identify or run time. A run-wise variable standardization was applied, before

670   model estimation, by de-meaning to zero and unit-variance scaling to one. The generalization

671   performance of the prediction accuracy was estimated via leave-one-subject-out cross-validation. In

672   total, 22 model instances were built from the brain data so that each subject's data were held out once

673   from the training process ('training') and exclusively used to assess the model's generalization

674   properties ('testing'). The parameters of the predictive algorithm were averaged across all cross-

675   validation folds to guard against noise and obtain a single aggregate predictive model solution for

676   inspection and visualization (Kernbach et al., 2018). The parameters of the predictive algorithm were

677   averaged across all cross-validation folds to guard against noise and obtain a single final predictive

678   model solution for inspection and visualization (Kernbach et al., 2018). The pattern-classification

679   pipelines were realized in the Python data science ecosystem, using especially nilearn v0.6.2

680   (Abraham et al., 2014) and scikit-learn v0.21.2 (Pedregosa et al., 2011). Overall, the set of

681   multivariate predictive analyses thus aimed at revealing task-distinctive information available at

682   subregion-level signals in our IPL ROIs.

683   **Task-evoked functional connectivity shifts**

684   We then quantitatively characterized the task-induced changes in distributed functional coupling

685   profiles as anchored in each of the IPL subregions. Analogous to the multivariate pattern recognition

686   approach (cf. last paragraph), this cortex-wide analysis was performed across the three distinct task

687   contexts. We drew on the commonly used Schaefer-Yeo atlas v0.15.3 (Schaefer et al., 2018) with 400

688   parcels to parse the distributed neural activity estimates (GLM_{trial}) of the three target conditions

689   (*invalid*, *word*, *false belief*). Consistent with the other analysis approaches, we discarded any trials

690   with incorrect subject responses. Neural activity estimates were summarized by averaging across all

691   voxels belonging to a given IPL subregion. For each experimental target condition, Pearson's

692 correlation coefficients were computed between a given IPL subregion and each of the Schaefer-Yeo

693 parcels. To rigorously assess whether connectivity links between a specific IPL subregion and cortical

694 parcel were reliably weaker or stronger in one task relative to the other two, a pooled permutation-

695 based baseline was computed across all three task conditions. Task-specific functional coupling shifts

696 were determined by statistical significance testing based on a non-parametric permutation procedure

697 using an empirical null-hypothesis distribution (Bzdok & Yeo, 2017). The data-derived null model

698 reflected the constellation of neural activity coupling strengths between a given subregion and other

699 cortical regions that would be expected if task A induced similar patterns of brain connectivity,

700 compared to the respective other tasks B and C. Following this fully data-driven analysis tactic, for

701 each of the three tasks, the analysis directly provided brain maps of task-dependent functional

702 connectivity profiles for the IPL subregions.

703 **Task-specific effective connectivity modulation**

704 After delineating (undirected) functional connectivity of IPL subregions with brain-wide cortical

705 regions, we explicitly examined task-dependent causal interactions within the IPL. To achieve this

706 goal, we analyzed the effective connectivity among the four IPL subregions by means of DCM. Since

707 this approach centered on the directed interaction among the IPL subregions themselves, this analysis

708 selectively included these four compartments. Effective connectivity was estimated with DCM 12.5

709 (Friston et al., 2013) implemented in SPM 12. We defined and deployed subject-wise DCMs with

710 one target node per subregion. Subject-specific node centers per subregion were based on the peak

711 activity across all three tasks. We ensured similar contribution of all tasks by task-wise normalization

712 of neural activity estimates to define the subject-wise DCM nodes. The first eigenvariate from the

713 timeseries of voxels in an 8mm sphere around this target was extracted (Zeidman et al., 2019). We

714 exclusively included data from voxels within the upper quartile of estimated neural activity to ensure

715 functional relevance (Seghier & Friston, 2013) and assured that all voxels fell into the respective IPL

716 subregion. A fully connected DCM (full model) estimated all possible connections among the four

717 IPL subregions (including self-connections) and directions of modulatory influences. The trial onsets
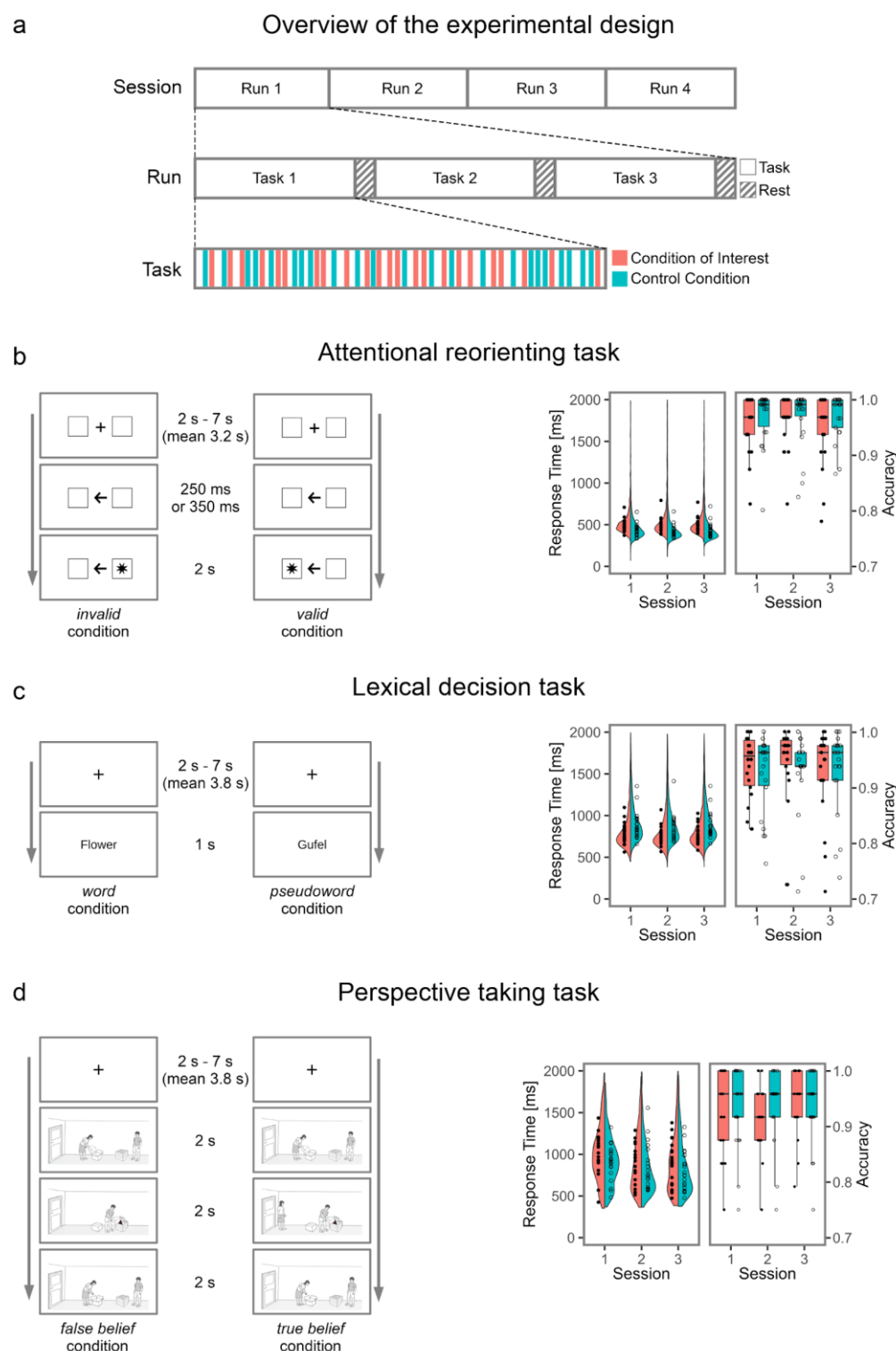
32

718   of the three target conditions were modeled as direct inputs to the nodes and as modulatory inputs to

719   the inter-regional connections. Neural activity stemming from incorrect trials and control conditions

720   was regressed out (Zeidman et al., 2019).

721   After model estimation, subject-wise full models were optimized for the intrinsic connections

722   (A matrix) and modulatory inputs (B matrix) at the group level using the Bayesian model selection

723   procedure (Friston & Penny, 2011). We decided against optimization of the input parameters (C

724   matrix), as we selectively modeled nodes in high-order association cortex. As such, there was no

725   obvious scientific hypothesis regarding the input to the system. The optimized, reduced model

726   represented fixed-effects at the group level (Rosa et al., 2012). As a second-level random-effects

727   analysis, we conducted a non-parametric permutation test on subject-wise parameters of the optimal

728   reduced model. This layer of analysis identified those model parameters that varied significantly

729   between tasks. Specifically, for each task, the parameter differences of the remaining two tasks were

730   randomly shuffled 10,000 times to obtain and test against an empirical distribution for the null

731   hypothesis (i.e., no differences between task-dependent effective connectivity). Statistical

732   significance was determined based on the absolute parameter difference higher than 99.9% of the

733   baseline difference, corresponding to $\alpha \leq 0.01$.

Acknowledgements

Supplementary Material

Figure 1–figure supplement 1. Experimental design and behavioral results. (a) **Experimental design.** Each of the four sessions consisted of four fMRI runs. In each run, all three tasks were presented in a pseudo-randomized order and analyzed in an event-related fashion. (b) **Attentional reorienting task.** In each trial, a directional arrow appeared at the center of the screen to direct the subject's attention to the left or right. In 75 % of the trials, the arrow correctly predicted the position of the target (*valid* condition), in 20 % of the trials,

753   the target appeared on the opposite side and subjects had to reorient their attention (*invalid* condition). In 5%

754   of the trials, no response was prompted (*catch* condition). Subjects indicated the side of the target via button

755   press. (**c**) **Lexical decision task**. Participants performed lexical decisions (*word* or *pseudoword* condition)

756   based on concrete German nouns or well matched pseudowords. (**d**) **Perspective taking task.** In each trial,

757   character A places a target object in a container. Thereafter, Character B changes the location of the target

758   object. Character A has left the room (*false belief* condition) or watches the relocation of the object (*true belief*

759   condition). Character A then searches for the target object at the location congruent with her / his knowledge

760   (*expected*) or at the contradicting location (*unexpected*). Participants had to indicate via button press whether

761   character A searched at the expected location or not. **Behavioral results** for each task are shown in the right

762   panel, separately for each session. Single subject data is overlaid as circles.

36

Hemispheric symmetry

763
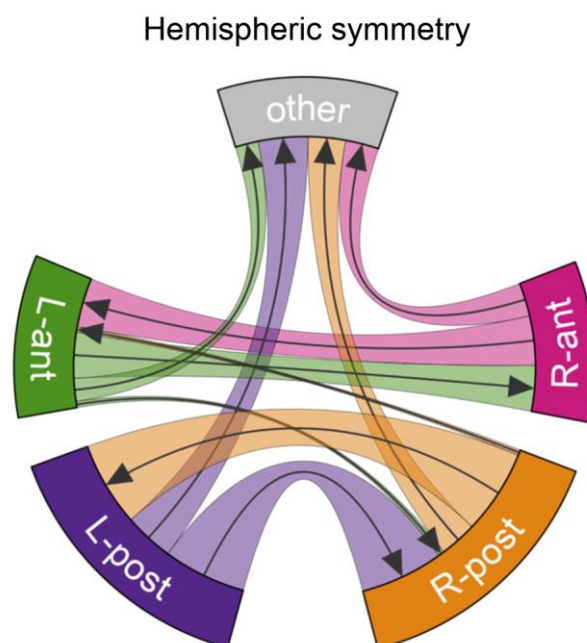
Figure 2–figure supplement 1. The final subregion solution shows a high degree of symmetry between hemispheres. Evidence supporting the hemispheric symmetry of the final two-subregion solution in the region of interest parcellation by clustering algorithms. Depicts which proportion of subregion-voxels falls into its homologue by flipping the x-axis, and which proportion falls into other areas.

IPL activity without motor responses

Attention

Semantics

Social Cognition

T-value

-8 -4 0 4 8
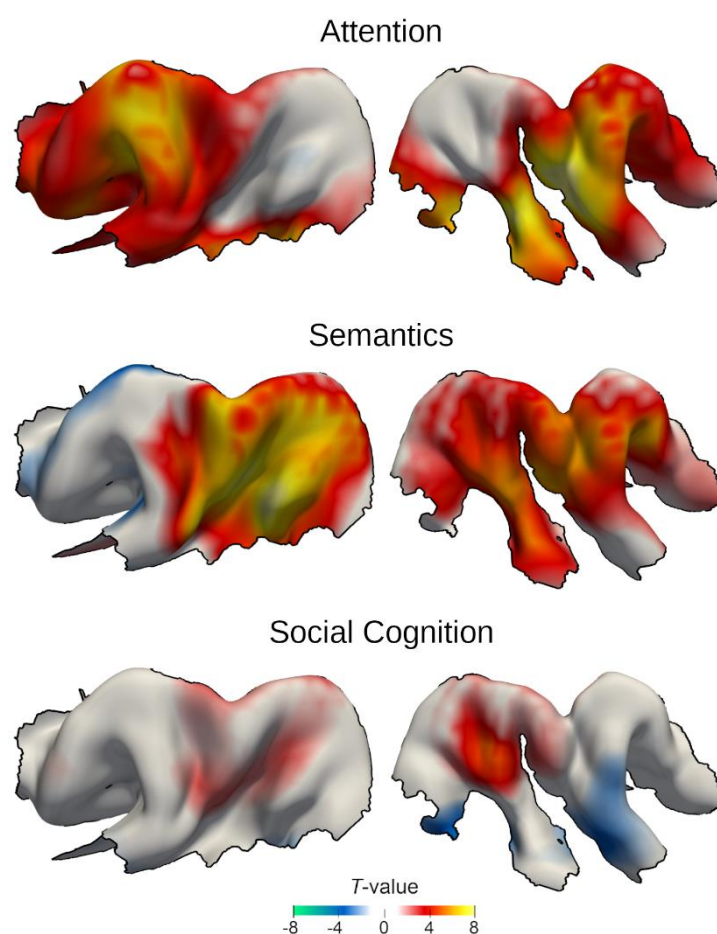
Figure 2–figure supplement 2. Task-evoked neural responses in the IPL region with explicit modelling of motor responses. Task-dependent BOLD responses from the model that explicitly accounts for general motor responses across tasks (GLM$_{cond+RT}$) resemble results from the original model (GLM$_{cond}$, Figure 1). Colors indicate unthresholded T-values. Warm colors: higher GLM beta estimates for the target conditions. Cold colors: higher GLM beta estimates for the control condition.

38
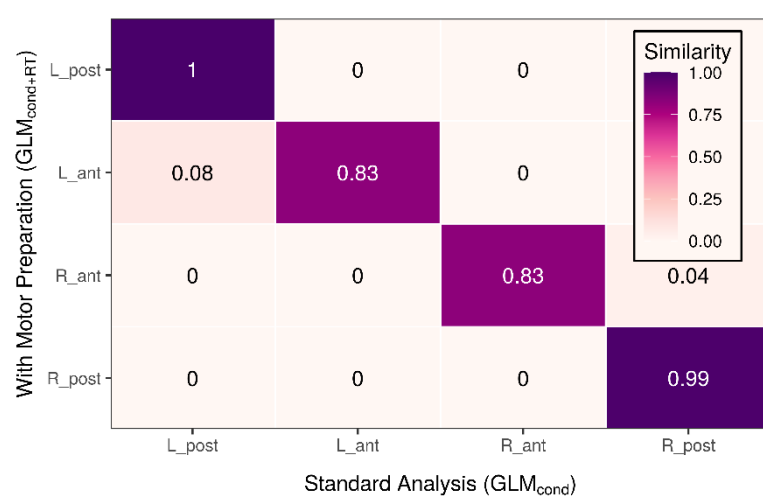
Figure 2–figure supplement 3. Explicitly modelling motor responses yields a similar clustering solution. Depicts the cluster-wise similarity of the parcellation solution based on the model that captured preparatory motor responses across tasks ($GLM_{cond+RT}$) compared to the basic model (GLM_{cond}).
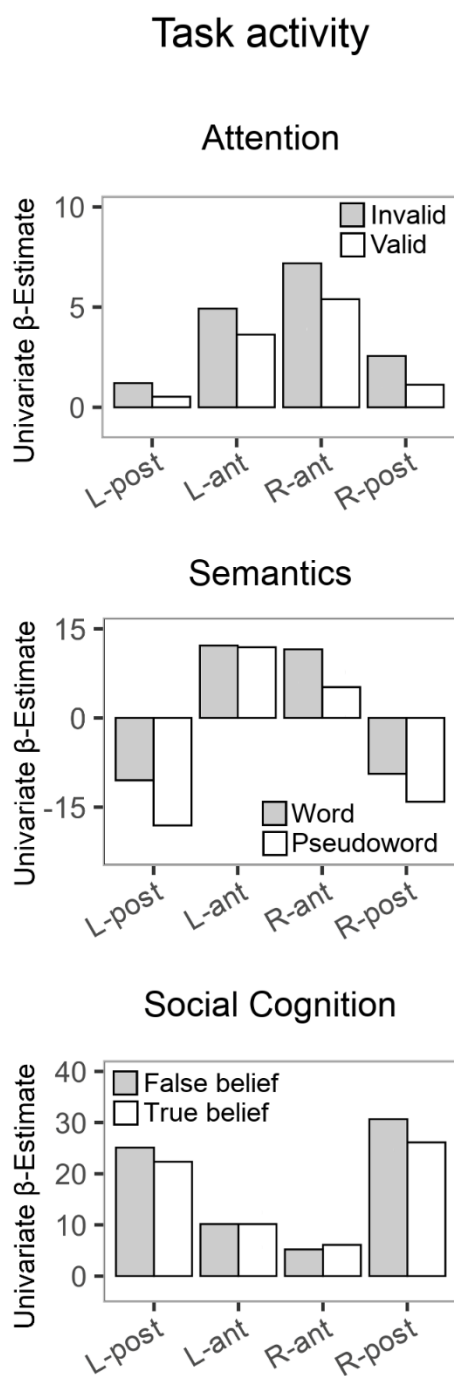
Task activity

Attention

Semantics

Social Cognition

778

779 **Figure 3–figure supplement 1. Neural activity estimates for the target and control conditions of the three**

780 **tasks.** For visualization purposes, beta estimates were extracted from GLM_{cond} at the center of mass for each

781 IPL subregion.

782

783
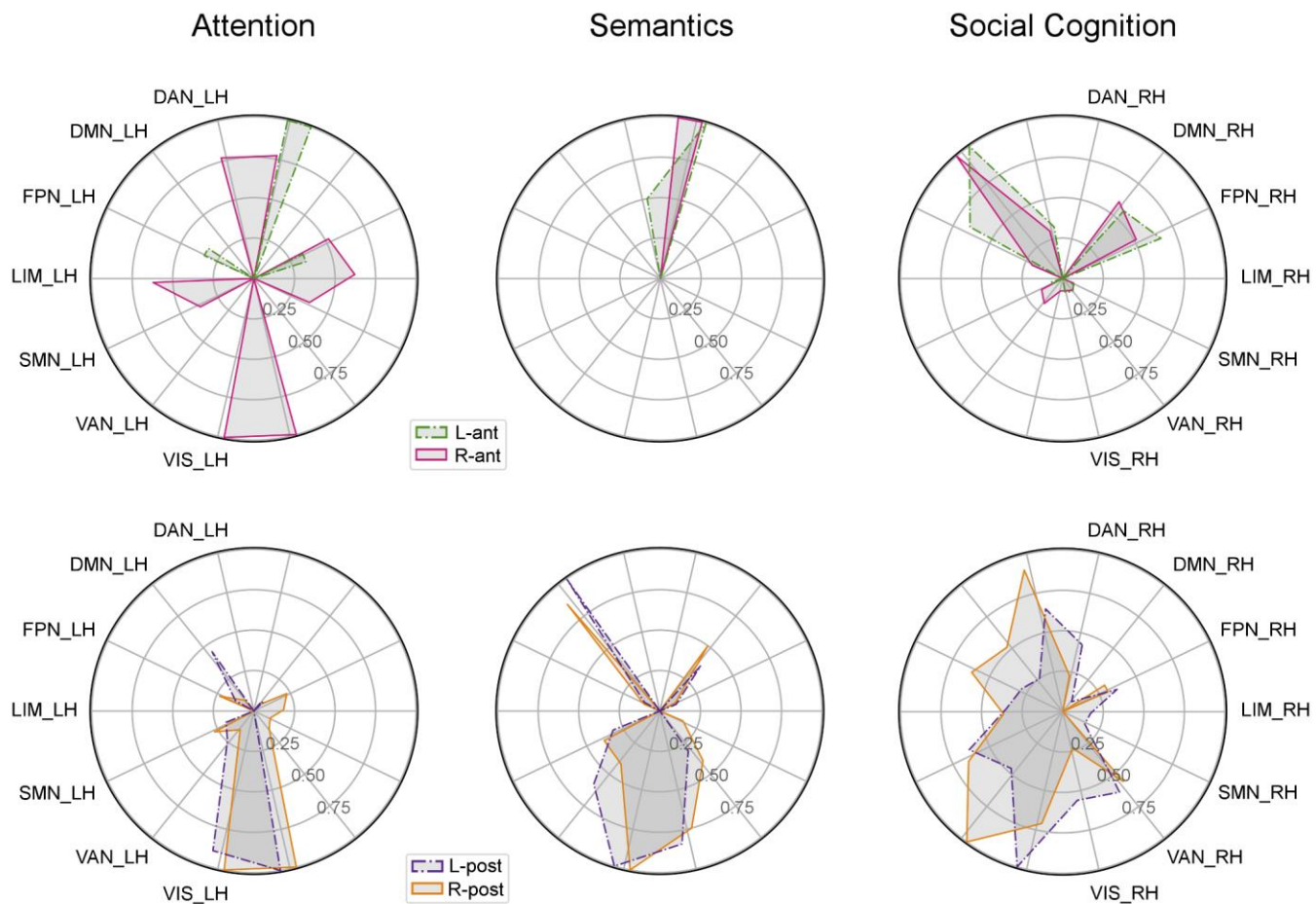
Figure 4–figure supplement 1. Functional connectivity between IPL subregions and large-scale brain networks. The preferred connectivity between IPL subregions and brain-wide cortical regions identified task-specific coupling motifs of the four subregions. Large-scale brain networks were split into their left and right hemispheric parts. Functional connectivity was normalized per subregion and task. Anterior IPL subregions (top row) connect in a hemisphere specific way, while posterior IPL subregions (bottom row) connect in a more bilateral-symmetric way. LH/RH: left/right hemispheric network parts. See main text for details on the connectivity metric. Networks acronyms as defined in the main text.

791 **Table S1**: Mass-univariate activations peaks for the three functional domains.

Region	Anatomical assignment	Hemisphere	X	Y	Z	T-value	Cluster size
Attentional reorienting							
Supramarginal gyrus	PFm	R	57	-48	24	9.68	181
Superior temporal gyrus / angular gyrus	PGa	R	63	-45	17	9.23	
Middle temporal gyrus / angular gyrus	PGp	R	48	-63	14	8.42	
Middle temporal gyrus		R	57	-57	-1	7.03	
Precuneus	7P	L	3	-54	52	9.46	123
Precuneus	5L	R	6	-60	59	8.27	
Precuneus	7A	L	12	-66	52	7.21	
Precentral gyrus		L	-27	-3	59	9.32	54
Superior frontal gyrus		R	30	-6	63	8.36	34
Middle frontal gyrus		R	36	-3	56	7.33	
Precentral gyrus		R	36	3	49	7.00	
Inferior parietal lobe	PF	L	-54	-42	38	7.35	33
Postcentral gyrus		L	-45	-33	49	7.04	
Inferior parietal lobule	hIP2	L	-45	-39	42	6.99	
Superior parietal lobe	hIP1	R	30	-48	42	10.10	31
Lexical decisions							
Angular gyrus	PGp	L	-51	-72	28	8.00	73
Angular gyrus	PGp	L	-39	-75	42	7.36	
Angular gyrus	PGa	L	-45	-57	35	7.22	
Middle cingulate gyrus	5M	L	-6	-30	42	9.07	50
Superior frontal gyrus		L	-18	36	49	7.94	34
Middle frontal gyrus		L	-27	24	52	6.64	
Perspective taking							
Supplementary motor cortex		L	-3	15	52	5.15	184
Superior medial gyrus		L	-6	24	42	4.37	
Superior frontal gyrus		L	-15	12	63	3.84	
Posterior medial frontal g.		R	12	6	52	3.73	
Inferior frontal gyrus	BA45	L	-45	24	31	5.11	59
Precentral gyrus		L	-39	3	42	4.77	45
not assigned		L	-45	6	56	3.84	
Precentral gyrus	BA44	L	-48	9	35	3.81	
Middle frontal gyrus		L	-42	3	52	3.72	
Angular gyrus	PGa	R	51	-60	31	5.15	32
Precuneus		R				4.50	31
Precuneus		L				3.98	
Middle temporal gyrus		R	54	-18	-15	4.68	20
Middle temporal gyrus		R	60	-15	-11	4.29	

792 *Note*: Attention and semantic tasks: thresholded at p=0.05, FWE corrected, cluster extent ≥20 voxels.
793 Social cognition task: thresholded at p=0.001, uncorrected, cluster extent ≥20 voxels. Anatomical
794 assignment according to SPM Anatomy toolbox (v. 22c).

795 **Table S2**: Intrinsic effective connectivity and task-specific self-connectivity modulation

Source subregion		Target subregion	Strength	95%-CI
Intrinsic connectivity				
L-ant	→	L-ant	-1.20	[-1.21; -1.20]
L-ant	→	L-post	-0.37	[-0.38; -0.37]
L-ant	→	R-ant	-0.33	[-0.33; -0.33]
L-ant	→	R-post	-0.56	[-0.56; -0.56]
L-post	→	L-ant	-0.05	[-0.06; -0.05]
L-post	→	L-post	-0.79	[-0.81; -0.79]
L-post	→	R-ant	0.15	[0.15; 0.16]
L-post	→	R-post	-0.29	[-0.29; -0.29]
R-ant	→	L-ant	-0.27	[-0.27; -0.27]
R-ant	→	L-post	0.38	[0.39; 0.39]
R-ant	→	R-ant	-1.13	[-1.14; -1.13]
R-ant	→	R-post	0.87	[0.87; 0.88]
R-post	→	L-ant	0.34	[0.34; 0.35]
R-post	→	L-post	0.42	[0.42; 0.43]
R-post	→	R-ant	-0.30	[-0.30; -0.30]
R-post	→	R-post	-1.14	[-1.15; -1.14]

Source subregion		Target subregion	Modulation strength	p-value
Self connectivity				
Semantics				
L-ant	→	L-ant	-5.53	0.0006
L-post	→	L-post	-6.88	0.0010
Social Cognition				
R-ant	→	R-ant	-4.01	0.0055

796 *Note:* Intrinsic connectivity parameters ('A-matrix') and significant modulatory parameters ('B-
797 matrix', α ≤ 0.01) of self-connections. Strength is given as posterior expectation from the optimum
798 Bayesian parameter average model. The 95% confidence intervals were built from the corresponding
799 Bayesian parameter covariances and exceed zero for all parameters. P-values for self-connectivity are
800 based on a random effects permutation test for the null hypothesis 'no parameter difference between
801 tasks'.

References

802

803 Abdulrahman, H., & Henson, R. N. (2016). Effect of trial-to-trial variability on optimal event-

804   related fMRI design: Implications for Beta-series correlation and multi-voxel pattern analysis.

805   *NeuroImage*, *125*, 756–766. https://doi.org/10.1016/j.neuroimage.2015.11.009

806 Abraham, A., Pedregosa, F., Eickenberg, M., Gervais, P., Mueller, A., Kossaifi, J., Gramfort, A.,

807   Thirion, B., & Varoquaux, G. (2014). Machine learning for neuroimaging with scikit-learn.

808   *Frontiers in Neuroinformatics*, *8*, 14. https://doi.org/10.3389/fninf.2014.00014

809 Ahrens, J., Geveci, B., & Law, C. (2005). ParaView: an end-user tool for large-data visualization.

810   In Hansen, C.D. & Johnson, C.R. (Ed.), *The Visualization Handbook* (pp. 717–731).

811   https://doi.org/10.1016/b978-012387582-2/50038-1

812 Amunts, K., & Zilles, K. (2001). Advances in cytoarchitectonic mapping of the human cerebral

813   cortex. *Neuroimaging Clinics of North America*, *11*(2), 151–169, vii.

814   https://www.ncbi.nlm.nih.gov/pubmed/11489732

815 Andersson, J. L. R., Skare, S., & Ashburner, J. (2003). How to correct susceptibility distortions in

816   spin-echo echo-planar images: application to diffusion tensor imaging. *NeuroImage*, *20*(2),

817   870–888. https://doi.org/10.1016/S1053-8119(03)00336-7

818 Avants, B. B., Epstein, C. L., Grossman, M., & Gee, J. C. (2008). Symmetric diffeomorphic image

819   registration with cross-correlation: evaluating automated labeling of elderly and

820   neurodegenerative brain. *Medical Image Analysis*, *12*(1), 26–41.

821   https://doi.org/10.1016/j.media.2007.06.004

822 Behzadi, Y., Restom, K., Liau, J., & Liu, T. T. (2007). A component based noise correction method

823   (CompCor) for BOLD and perfusion based fMRI. *NeuroImage*, *37*(1), 90–101.

824   https://doi.org/10.1016/j.neuroimage.2007.04.042

825 Binder, J. R., & Desai, R. H. (2011). The neurobiology of semantic memory. *Trends Cog. Sci.*,

826   *15*(11), 527–536. https://doi.org/10.1016/j.tics.2011.10.001

827 Binder, J. R., Desai, R. H., Graves, W. W., & Conant, L. L. (2009). Where Is the semantic system?

828   A critical review and meta-analysis of 120 functional neuroimaging studies. *Cereb. Cortex*,

829   *19*(12), 2767–2796. https://doi.org/10.1093/cercor/bhp055

830   Binder, J. R., McKiernan, K. A., Parsons, M. E., Westbury, C. F., Possing, E. T., Kaufman, J. N., &

831   Buchanan, L. (2003). Neural correlates of lexical access during visual word recognition.

832   *Journal of Cognitive Neuroscience*, *15*(3), 372–393.

833   https://doi.org/10.1162/089892903321593108

834   Braga, R. M., DiNicola, L. M., & Buckner, R. L. (2019). Situating the left-lateralized language

835   network in the broader organization of multiple specialized large-scale distributed networks. In

836   *bioRxiv*. https://doi.org/10.1101/2019.12.11.873174

837   Brysbaert, M., Buchmeier, M., Conrad, M., Jacobs, A. M., Bölte, J., & Böhl, A. (2011). The word

838   frequency effect: a review of recent developments and implications for the choice of frequency

839   estimates in German. *Experimental Psychology*, *58*(5), 412–424. https://doi.org/10.1027/1618-

840   3169/a000123

841   Buckner, R. L., & DiNicola, L. M. (2019). The brain's default network: updated anatomy,

842   physiology and evolving insights. *Nat. Rev. Neurosci.*, *20*(10), 593–608.

843   https://doi.org/10.1038/s41583-019-0212-7

844   Bzdok, D., Hartwigsen, G., Reid, A., Laird, A. R., Fox, P. T., & Eickhoff, S. B. (2016). Left inferior

845   parietal lobe engagement in social cognition and language. *Neuroscience and Biobehavioral*

846   *Reviews*, *68*, 319–334. https://doi.org/10.1016/j.neubiorev.2016.02.024

847   Bzdok, D., Langner, R., Schilbach, L., Jakobs, O., Roski, C., Caspers, S., Laird, A. R., Fox, P. T.,

848   Zilles, K., & Eickhoff, S. B. (2013). Characterization of the temporo-parietal junction by

849   combining data-driven parcellation, complementary connectivity analyses, and functional

850   decoding. *NeuroImage*, *81*, 381–392. https://doi.org/10.1016/j.neuroimage.2013.05.046

851   Bzdok, D., & Yeo, B. T. T. (2017). Inference in the age of big data: Future perspectives on

852   neuroscience. *NeuroImage*, *155*, 549–564. https://doi.org/10.1016/j.neuroimage.2017.04.061

853   Caspers, S., Eickhoff, S. B., Geyer, S., Scheperjans, F., Mohlberg, H., Zilles, K., & Amunts, K.

854   (2008). The human inferior parietal lobule in stereotaxic space. *Brain Structure & Function*,

855   *212*(6), 481–495. https://doi.org/10.1007/s00429-008-0195-z

856 Caspers, S., Eickhoff, S. B., Rick, T., von Kapri, A., Kuhlen, T., Huang, R., Shah, N. J., & Zilles,

857   K. (2011). Probabilistic fibre tract analysis of cytoarchitectonically defined human inferior

858   parietal lobule areas reveals similarities to macaques. *NeuroImage*, *58*(2), 362–380.

859   https://doi.org/10.1016/j.neuroimage.2011.06.027

860 Chafee, M. V., Averbeck, B. B., & Crowe, D. A. (2007). Representing spatial relationships in

861   posterior parietal cortex: single neurons code object-referenced position. *Cerebral Cortex* ,

862   *17*(12), 2914–2932. https://doi.org/10.1093/cercor/bhm017

863 Charrad, M., Ghazzali, N., Boiteau, V., & Niknafs, A. (2014). NbClust: An R package for

864   determining the relevant number of clusters in a data set. *J. Stat. Softw.*, *61*(6), 1–36.

865   https://doi.org/10.18637/jss.v061.i06

866 Corbetta, M., Patel, G., & Shulman, G. L. (2008). The reorienting system of the human brain: from

867   environment to theory of mind. *Neuron*, *58*(3), 306–324.

868   https://doi.org/10.1016/j.neuron.2008.04.017

869 Corbetta, M., Ramsey, L., Callejas, A., Baldassarre, A., Hacker, C. D., Siegel, J. S., Astafiev, S. V.,

870   Rengachary, J., Zinn, K., Lang, C. E., Connor, L. T., Fucetola, R., Strube, M., Carter, A. R., &

871   Shulman, G. L. (2015). Common behavioral clusters and subcortical anatomy in stroke.

872   *Neuron*, *85*(5), 927–941. https://doi.org/10.1016/j.neuron.2015.02.027

873 Corbin, N., Todd, N., Friston, K. J., & Callaghan, M. F. (2018). Accurate modeling of temporal

874   correlations in rapidly sampled fMRI time series. *Human Brain Mapping*, *39*(10), 3884–3897.

875   https://doi.org/10.1002/hbm.24218

876 Cox, R. W. (1996). AFNI: software for analysis and visualization of functional magnetic resonance

877   neuroimages. *Computers and Biomedical Research, an International Journal*, *29*(3), 162–173.

878   https://doi.org/10.1006/cbmr.1996.0014

879 Crowe, D. A., Averbeck, B. B., & Chafee, M. V. (2008). Neural ensemble decoding reveals a

880   correlate of viewer- to object-centered spatial transformation in monkey parietal cortex. *The*

881   *Journal of Neuroscience: The Official Journal of the Society for Neuroscience*, *28*(20), 5218–

882   5228. https://doi.org/10.1523/JNEUROSCI.5105-07.2008

883 Crowe, D. A., Averbeck, B. B., Chafee, M. V., & Georgopoulos, A. P. (2005). Dynamics of parietal

884   neural activity during spatial cognitive processing. *Neuron*, *47*(6), 885–891.

885   https://doi.org/10.1016/j.neuron.2005.08.005

886 Crowe, D. A., Chafee, M. V., Averbeck, B. B., & Georgopoulos, A. P. (2004). Neural activity in

887   primate parietal area 7a related to spatial analysis of visual mazes. *Cerebral Cortex* , *14*(1),

888   23–34. https://doi.org/10.1093/cercor/bhg088

889 Dale, A. M., Fischl, B., & Sereno, M. I. (1999). Cortical surface-based analysis. I. Segmentation

890   and surface reconstruction. *NeuroImage*, *9*(2), 179–194.

891   https://doi.org/10.1006/nimg.1998.0395

892 Dronkers, N. F., Wilkins, D. P., Van Valin, R. D., Jr, Redfern, B. B., & Jaeger, J. J. (2004). Lesion

893   analysis of the brain areas involved in language comprehension. *Cognition*, *92*(1-2), 145–177.

894   https://doi.org/10.1016/j.cognition.2003.11.002

895 Durnez, J., Blair, R., & Poldrack, R. A. (2018). Neurodesign: optimal experimental designs for task

896   fMRI. In *bioRxiv*. https://doi.org/10.1101/119594

897 Eickhoff, S. B., Stephan, K. E., Mohlberg, H., Grefkes, C., Fink, G. R., Amunts, K., & Zilles, K.

898   (2005). A new SPM toolbox for combining probabilistic cytoarchitectonic maps and functional

899   imaging data. *NeuroImage*, *25*(4), 1325–1335.

900   https://doi.org/10.1016/j.neuroimage.2004.12.034

901 Esteban, O., Markiewicz, C. J., Blair, R. W., Moodie, C. A., Isik, A. I., Erramuzpe, A., Kent, J. D.,

902   Goncalves, M., DuPre, E., Snyder, M., Oya, H., Ghosh, S. S., Wright, J., Durnez, J., Poldrack,

903   R. A., & Gorgolewski, K. J. (2019). fMRIPrep: a robust preprocessing pipeline for functional

904   MRI. *Nature Methods*, *16*(1), 111–116. https://doi.org/10.1038/s41592-018-0235-4

905 Feinberg, D. A., Moeller, S., Smith, S. M., Auerbach, E., Ramanna, S., Gunther, M., Glasser, M. F.,

906   Miller, K. L., Ugurbil, K., & Yacoub, E. (2010). Multiplexed echo planar imaging for sub-

907   second whole brain FMRI and fast diffusion imaging. *PloS One*, *5*(12), e15710.

908   https://doi.org/10.1371/journal.pone.0015710

909 Fischl, B., Sereno, M. I., Tootell, R. B. H., & Dale, A. M. (1999). High-resolution intersubject

910   averaging and a coordinate system for the cortical surface. *Hum. Brain Mapp.*, *8*(4), 272–284.

911   https://doi.org/3.0.co;2-4">10.1002/(sici)1097-0193(1999)8:4<272::aid-hbm10>3.0.co;2-4

912 Fogassi, L., Ferrari, P. F., Gesierich, B., Rozzi, S., Chersi, F., & Rizzolatti, G. (2005). Parietal lobe:

913   from action organization to intention understanding. *Science*, *308*(5722), 662–667.

914   https://doi.org/10.1126/science.1106138

915 Fonov, V. S., Evans, A. C., McKinstry, R. C., Almli, C. R., & Collins, D. L. (2009). Unbiased

916   nonlinear average age-appropriate brain templates from birth to adulthood. *Neuroimage*, *47*,

917   S102. https://doi.org/10.1016/s1053-8119(09)70884-5

918 Fridriksson, J., Kjartansson, O., Morgan, P. S., Hjaltason, H., Magnusdottir, S., Bonilha, L., &

919   Rorden, C. (2010). Impaired speech repetition and left parietal lobe damage. *The Journal of*

920   *Neuroscience: The Official Journal of the Society for Neuroscience*, *30*(33), 11057–11061.

921   https://doi.org/10.1523/JNEUROSCI.1120-10.2010

922 Fridriksson, J., Yourganov, G., Bonilha, L., Basilakos, A., Den Ouden, D.-B., & Rorden, C. (2016).

923   Revealing the dual streams of speech processing. *Proceedings of the National Academy of*

924   *Sciences of the United States of America*, *113*(52), 15108–15113.

925   https://doi.org/10.1073/pnas.1614038114

926 Friederici, A. D. (2017). Evolution of the neural language network. *Psychon Bull. Rev.*, *24*(1), 41–

927   47. https://doi.org/10.3758/s13423-016-1090-x

928 Friston, K., Moran, R., & Seth, A. K. (2013). Analysing connectivity with Granger causality and

929   dynamic causal modelling. *Current Opinion in Neurobiology*, *23*(2), 172–178.

930   https://doi.org/10.1016/j.conb.2012.11.010

931 Friston, K., & Penny, W. (2011). Post hoc Bayesian model selection. *NeuroImage*, *56*(4), 2089–

932   2099. https://doi.org/10.1016/j.neuroimage.2011.03.062

933   Fukuda, H., Ma, N., Suzuki, S., Harasawa, N., Ueno, K., Gardner, J. L., Ichinohe, N., Haruno, M.,

934   Cheng, K., & Nakahara, H. (2019). Computing social value conversion in the human brain.

935   *The Journal of Neuroscience: The Official Journal of the Society for Neuroscience*, *39*(26),

936   5153–5172. https://doi.org/10.1523/JNEUROSCI.3117-18.2019

937   Gordon, E. M., Laumann, T. O., Marek, S., Raut, R. V., Gratton, C., Newbold, D. J., Greene, D. J.,

938   Coalson, R. S., Snyder, A. Z., Schlaggar, B. L., Petersen, S. E., Dosenbach, N. U. F., &

939   Nelson, S. M. (2020). Default-mode network streams for coupling to language and control

940   systems. *Proceedings of the National Academy of Sciences of the United States of America*.

941   https://doi.org/10.1073/pnas.2005238117

942   Gorgolewski, K., Burns, C. D., Madison, C., Clark, D., Halchenko, Y. O., Waskom, M. L., &

943   Ghosh, S. S. (2011). Nipype: a flexible, lightweight and extensible neuroimaging data

944   processing framework in python. *Frontiers in Neuroinformatics*, *5*, 13.

945   https://doi.org/10.3389/fninf.2011.00013

946   Greve, D. N., & Fischl, B. (2009). Accurate and robust brain image alignment using boundary-

947   based registration. *NeuroImage*, *48*(1), 63–72.

948   https://doi.org/10.1016/j.neuroimage.2009.06.060

949   Gu, Z., Gu, L., Eils, R., Schlesner, M., & Brors, B. (2014). circlize implements and enhances

950   circular visualization in R. *Bioinformatics*, *30*(19), 2811–2812.

951   https://doi.org/10.1093/bioinformatics/btu393

952   Hartigan, J. A., & Wong, M. A. (1979). Algorithm AS 136: A K-Means Clustering Algorithm. *J.

953   Appl. Stat.*, *28*(1), 100. https://doi.org/10.2307/2346830

954   Hartwigsen, G. (2018). Flexible Redistribution in Cognitive Networks. *Trends Cogn. Sci.*, *22*(8),

955   687–698. https://doi.org/10.1016/j.tics.2018.05.008

956   Hartwigsen, G., Bzdok, D., Klein, M., Wawrzyniak, M., Stockert, A., Wrede, K., Classen, J., &

957   Saur, D. (2017). Rapid short-term reorganization in the language network. *eLife*, *6*, 1–18.

958   https://doi.org/10.7554/eLife.25964

959   Hartwigsen, G., Stockert, A., Charpentier, L., Wawrzyniak, M., Klingbeil, J., Wrede, K., Obrig, H.,

960   & Saur, D. (2020). Short-term modulation of the lesioned language network. *eLife*, *9*.

961   https://doi.org/10.7554/eLife.54277

962   Hartwigsen, G., Weigel, A., Schuschan, P., Siebner, H. R., Weise, D., Classen, J., & Saur, D.

963   (2016). Dissociating parieto-frontal networks for phonological and semantic word decisions: A

964   condition-and-perturb TMS study. *Cerebral Cortex*, *26*(6), 2590–2601.

965   https://doi.org/10.1093/cercor/bhv092

966   Igelström, K. M., Webb, T. W., Kelly, Y. T., & Graziano, M. S. A. (2016). Topographical

967   organization of attentional, social, and memory processes in the human temporoparietal cortex.

968   *eNeuro*, *3*(2), 1–12. https://doi.org/10.1523/ENEURO.0060-16.2016

969   Jenkinson, M., Bannister, P., Brady, M., & Smith, S. (2002). Improved optimization for the robust

970   and accurate linear registration and motion correction of brain images. *NeuroImage*, *17*(2),

971   825–841. https://doi.org/10.1016/s1053-8119(02)91132-8

972   Kanske, P., & Kotz, S. A. (2011). Cross-modal validation of the Leipzig Affective Norms for

973   German (LANG). *Behavior Research Methods*, *43*(2), 409–413.

974   https://doi.org/10.3758/s13428-010-0048-6

975   Kernbach, J. M., Yeo, B. T. T., Smallwood, J., Margulies, D. S., Thiebaut de Schotten, M., Walter,

976   H., Sabuncu, M. R., Holmes, A. J., Gramfort, A., Varoquaux, G., Thirion, B., & Bzdok, D.

977   (2018). Subspecialization within default mode nodes characterized in 10,000 UK Biobank

978   participants. *Proceedings of the National Academy of Sciences of the United States of America*,

979   *115*(48), 12295–12300. https://doi.org/10.1073/pnas.1804876115

980   Keuleers, E., & Brysbaert, M. (2010). Wuggy: a multilingual pseudoword generator. *Behavior*

981   *Research Methods*, *42*(3), 627–633. https://doi.org/10.3758/BRM.42.3.627

982   Klein, A., Ghosh, S. S., Bao, F. S., Giard, J., Häme, Y., Stavsky, E., Lee, N., Rossa, B., Reuter, M.,

983   Chaibub Neto, E., & Keshavan, A. (2017). Mindboggling morphometry of human brains. *PLoS*

984   *Computational Biology*, *13*(2), e1005350. https://doi.org/10.1371/journal.pcbi.1005350

985   Krall, S. C., Volz, L. J., Oberwelland, E., Grefkes, C., Fink, G. R., & Konrad, K. (2016). The right

986   temporoparietal junction in attention and social interaction: a transcranial magnetic stimulation

987   study. *Human Brain Mapping*, *37*(2), 796–807. https://doi.org/10.1002/hbm.23068

988   Kravitz, D. J., Saleem, K. S., Baker, C. I., & Mishkin, M. (2011). A new neural framework for

989   visuospatial processing. *Nature Reviews. Neuroscience*, *12*(4), 217–230.

990   https://doi.org/10.1038/nrn3008

991   Lambon Ralph, M. A., & Patterson, K. (2008). Generalization and differentiation in semantic

992   memory: insights from semantic dementia. *Annals of the New York Academy of Sciences*,

993   *1124*, 61–76. https://doi.org/10.1196/annals.1440.006

994   Marcus, D. S., Wang, T. H., Parker, J., Csernansky, J. G., Morris, J. C., & Buckner, R. L. (2007).

995   Open Access Series of Imaging Studies (OASIS): cross-sectional MRI data in young, middle

996   aged, nondemented, and demented older adults. *Journal of Cognitive Neuroscience*, *19*(9),

997   1498–1507. https://doi.org/10.1162/jocn.2007.19.9.1498

998   Margulies, D. S., Ghosh, S. S., Goulas, A., Falkiewicz, M., Huntenburg, J. M., Langs, G., Bezgin,

999   G., Eickhoff, S. B., Castellanos, F. X., Petrides, M., Jefferies, E., & Smallwood, J. (2016).

1000   Situating the default-mode network along a principal gradient of macroscale cortical

1001   organization. *Proceedings of the National Academy of Sciences of the United States of*

1002   *America*, *113*(44), 12574–12579. https://doi.org/10.1073/pnas.1608282113

1003   Mars, R. B., Jbabdi, S., Sallet, J., O'Reilly, J. X., Croxson, P. L., Olivier, E., Noonan, M. P.,

1004   Bergmann, C., Mitchell, A. S., Baxter, M. G., Behrens, T. E. J., Johansen-Berg, H., Tomassini,

1005   V., Miller, K. L., & Rushworth, M. F. S. (2011). Diffusion-weighted imaging tractography-

1006   based parcellation of the human parietal cortex and comparison with human and macaque

1007   resting-state functional connectivity. *J. Neurosci.*, *31*(11), 4087–4100.

1008   https://doi.org/10.1523/jneurosci.5102-10.2011

1009   Mars, R. B., Sallet, J., Neubert, F.-X., & Rushworth, M. F. S. (2013). Connectivity profiles reveal

1010　　　　the relationship between brain areas for social cognition in human and monkey temporoparietal

1011　　　　cortex. *Proceedings of the National Academy of Sciences of the United States of America*,

1012　　　　*110*(26), 10806–10811. https://doi.org/10.1073/pnas.1302956110

1013　　Mazziotta, J., Toga, A., Evans, A., Fox, P., Lancaster, J., Zilles, K., Woods, R., Paus, T., Simpson,

1014　　　　G., Pike, B., Holmes, C., Collins, L., Thompson, P., MacDonald, D., Iacoboni, M.,

1015　　　　Schormann, T., Amunts, K., Palomero-Gallagher, N., Geyer, S., … Mazoyer, B. (2001). A

1016　　　　probabilistic atlas and reference system for the human brain: International Consortium for

1017　　　　Brain Mapping (ICBM). *Philosophical Transactions of the Royal Society of London. Series B,*

1018　　　　*Biological Sciences*, *356*(1412), 1293–1322. https://doi.org/10.1098/rstb.2001.0915

1019　　Mirman, D., & Graziano, K. M. (2012). Damage to temporo-parietal cortex decreases incidental

1020　　　　activation of thematic relations during spoken word comprehension. *Neuropsychologia*, *50*(8),

1021　　　　1990–1997. https://doi.org/10.1016/j.neuropsychologia.2012.04.024

1022　　Morrow, L. A., & Ratcliff, G. (1998). The disengagement of covert attention and the neglect

1023　　　　syndrome. *Psychobiology* , *16*(3), 261–269.

1024　　Oldfield, R. C. (1971). The assessment and analysis of handedness: the Edinburgh inventory.

1025　　　　*Neuropsychologia*, *9*(1), 97–113. https://doi.org/10.1016/0028-3932(71)90067-4

1026　　Oligschläger, S., Xu, T., Baczkowski, B. M., Falkiewicz, M., Falchier, A., Linn, G., & Margulies,

1027　　　　D. S. (2018). Gradients of connectivity distance in the cerebral cortex of the macaque monkey.

1028　　　　*Brain Structure & Function*, *224*, 925–935. https://doi.org/10.1101/467860

1029　　Orban, G. A., Van Essen, D., & Vanduffel, W. (2004). Comparative mapping of higher visual areas

1030　　　　in monkeys and humans. *Trends in Cognitive Sciences*, *8*(7), 315–324.

1031　　　　https://doi.org/10.1016/j.tics.2004.05.009

1032　　Pedregosa, F., Varoquaux, G., Gramfort, A., Michel, V., Thirion, B., Grisel, O., Blondel, M.,

1033　　　　Prettenhofer, P., Weiss, R., Dubourg, V., Vanderplas, J., Passos, A., Cournapeau, D., Brucher,

1034　　　　M., Perrot, M., & Duchesnay, E. (2011). Scikit-learn: machine Learning in Python. *Journal of*

1035　　　　*Machine Learning Research: JMLR*, *12*, 2825–2830.

1036   Power, J. D., Barnes, K. A., Snyder, A. Z., Schlaggar, B. L., & Petersen, S. E. (2012). Spurious but

1037   systematic correlations in functional connectivity MRI networks arise from subject motion.

1038   *NeuroImage*, *59*(3), 2142–2154. https://doi.org/10.1016/j.neuroimage.2011.10.018

1039   Power, J. D., Mitra, A., Laumann, T. O., Snyder, A. Z., Schlaggar, B. L., & Petersen, S. E. (2014).

1040   Methods to detect, characterize, and remove motion artifact in resting state fMRI. *NeuroImage*,

1041   *84*, 320–341. https://doi.org/10.1016/j.neuroimage.2013.08.048

1042   Rosa, M. J., Friston, K., & Penny, W. (2012). Post-hoc selection of dynamic causal models. *Journal

1043   of Neuroscience Methods*, *208*(1), 66–78. https://doi.org/10.1016/j.jneumeth.2012.04.013

1044   Rothmayr, C., Sodian, B., Hajak, G., Döhnel, K., Meinhardt, J., & Sommer, M. (2011). Common

1045   and distinct neural networks for false-belief reasoning and inhibitory control. *NeuroImage*,

1046   *56*(3), 1705–1713. https://doi.org/10.1016/j.neuroimage.2010.12.052

1047   Rozzi, S., Ferrari, P. F., Bonini, L., Rizzolatti, G., & Fogassi, L. (2008). Functional organization of

1048   inferior parietal lobule convexity in the macaque monkey: electrophysiological

1049   characterization of motor, sensory and mirror responses and their correlation with

1050   cytoarchitectonic areas. *The European Journal of Neuroscience*, *28*(8), 1569–1588.

1051   https://doi.org/10.1111/j.1460-9568.2008.06395.x

1052   Rushworth, M. F., Ellison, A., & Walsh, V. (2001). Complementary localization and lateralization

1053   of orienting and motor attention. *Nature Neuroscience*, *4*(6), 656–661.

1054   https://doi.org/10.1038/88492

1055   Samson, D., Apperly, I. A., Chiavarino, C., & Humphreys, G. W. (2004). Left temporoparietal

1056   junction is necessary for representing someone else's belief. *Nat. Neurosci.*, *7*(5), 499–500.

1057   https://doi.org/10.1038/nn1223

1058   Schaefer, A., Kong, R., Gordon, E. M., Laumann, T. O., Zuo, X.-N., Holmes, A. J., Eickhoff, S. B.,

1059   & Yeo, B. T. T. (2018). Local-global parcellation of the human cerebral cortex from intrinsic

1060   functional connectivity MRI. *Cerebral Cortex* , *28*(9), 3095–3114.

1061   https://doi.org/10.1093/cercor/bhx179

1062 Schuwerk, T., Schurz, M., Müller, F., Rupprecht, R., & Sommer, M. (2017). The rTPJ's

1063   overarching cognitive function in networks for attention and theory of mind. *Soc. Cogn. Affect.*

1064   *Neurosci.*, *12*(1), 157–168. https://doi.org/10.1093/scan/nsw163

1065 Schwartz, M. F., Kimberg, D. Y., Walker, G. M., Brecher, A., Faseyitan, O. K., Dell, G. S.,

1066   Mirman, D., & Coslett, H. B. (2011). Neuroanatomical dissociation for taxonomic and

1067   thematic knowledge in the human brain. *Proceedings of the National Academy of Sciences of*

1068   *the United States of America*, *108*(20), 8520–8524. https://doi.org/10.1073/pnas.1014935108

1069 Seghier, M. L. (2013). The angular gyrus: multiple functions and multiple subdivisions. *The*

1070   *Neuroscientist: A Review Journal Bringing Neurobiology, Neurology and Psychiatry*, *19*(1),

1071   43–61. https://doi.org/10.1177/1073858412440596

1072 Seghier, M. L., & Friston, K. J. (2013). Network discovery with large DCMs. *NeuroImage*, *68*,

1073   181–191. https://doi.org/10.1016/j.neuroimage.2012.12.005

1074 Sliwinska, M. W., James, A., & Devlin, J. T. (2015). Inferior parietal lobule contributions to visual

1075   word recognition. *Journal of Cognitive Neuroscience*, *27*(3), 593–604.

1076   https://doi.org/10.1162/jocn_a_00721

1077 Snyder, L. H., Grieve, K. L., Brotchie, P., & Andersen, R. A. (1998). Separate body- and world-

1078   referenced representations of visual space in parietal cortex. *Nature*, *394*(6696), 887–891.

1079   https://doi.org/10.1038/29777

1080 Sommer, M., Meinhardt, J., Eichenmüller, K., Sodian, B., Döhnel, K., & Hajak, G. (2010).

1081   Modulation of the cortical false belief network during development. *Brain Research*, *1354*,

1082   123–131. https://doi.org/10.1016/j.brainres.2010.07.057

1083 Thiebaut de Schotten, M., Tomaiuolo, F., Aiello, M., Merola, S., Silvetti, M., Lecce, F.,

1084   Bartolomeo, P., & Doricchi, F. (2014). Damage to white matter pathways in subacute and

1085   chronic spatial neglect: a group study and 2 single-case studies with complete virtual "in vivo"

1086   tractography dissection. *Cerebral Cortex* , *24*(3), 691–706.

1087   https://doi.org/10.1093/cercor/bhs351

1088   Thirion, B., Varoquaux, G., Dohmatob, E., & Poline, J.-B. (2014). Which fMRI clustering gives

1089   good brain parcellations? *Frontiers in Neuroscience*, *8*, 167.

1090   https://doi.org/10.3389/fnins.2014.00167

1091   Toga, A. W., & Thompson, P. M. (2003). Mapping brain asymmetry. *Nature Reviews.*

1092   *Neuroscience*, *4*(1), 37–48. https://doi.org/10.1038/nrn1009

1093   Tustison, N. J., Avants, B. B., Cook, P. A., Zheng, Y., Egan, A., Yushkevich, P. A., & Gee, J. C.

1094   (2010). N4ITK: improved N3 bias correction. *IEEE Transactions on Medical Imaging*, *29*(6),

1095   1310–1320. https://doi.org/10.1109/TMI.2010.2046908

1096   Van Essen, D. C., & Dierker, D. L. (2007). Surface-based and probabilistic atlases of primate

1097   cerebral cortex. *Neuron*, *56*(2), 209–225. https://doi.org/10.1016/j.neuron.2007.10.015

1098   Vázquez-Rodríguez, B., Suárez, L. E., Markello, R. D., Shafiei, G., Paquola, C., Hagmann, P., van

1099   den Heuvel, M. P., Bernhardt, B. C., Nathan Spreng, R., & Misic, B. (2019). Gradients of

1100   structure–function tethering across neocortex. *Proceedings of the National Academy of*

1101   *Sciences of the United States of America*, *116*(42), 21219–21227.

1102   https://doi.org/10.1073/pnas.1903403116

1103   Wu, J., Ngo, G. H., Greve, D., Li, J., He, T., Fischl, B., Eickhoff, S. B., & Yeo, B. T. T. (2018).

1104   Accurate nonlinear mapping between MNI volumetric and FreeSurfer surface coordinate

1105   systems. *Human Brain Mapping*, *39*(9), 3793–3808. https://doi.org/10.1002/hbm.24213

1106   Xia, M., Wang, J., & He, Y. (2013). BrainNet Viewer: a network visualization tool for human brain

1107   connectomics. *PloS One*, *8*(7), e68910. https://doi.org/10.1371/journal.pone.0068910

1108   Xu, T., Nenning, K.-H., Schwartz, E., Hong, S.-J., Vogelstein, J. T., Goulas, A., Fair, D. A.,

1109   Schroeder, C. E., Margulies, D. S., Smallwood, J., Milham, M. P., & Langs, G. (2020). Cross-

1110   species functional alignment reveals evolutionary hierarchy within the connectome.

1111   *NeuroImage*, *223*, 117346. https://doi.org/10.1016/j.neuroimage.2020.117346

1112   Yeo, B. T. T., Krienen, F. M., Sepulcre, J., Sabuncu, M. R., Lashkari, D., Hollinshead, M.,

1113   Roffman, J. L., Smoller, J. W., Zöllei, L., Polimeni, J. R., Fischl, B., Liu, H., & Buckner, R. L.

1114   (2011). The organization of the human cerebral cortex estimated by intrinsic functional

1115   connectivity. *Journal of Neurophysiology*, *106*(3), 1125–1165.

1116   https://doi.org/10.1152/jn.00338.2011

1117   Zeidman, P., Jafarian, A., Corbin, N., Seghier, M. L., Razi, A., Price, C. J., & Friston, K. J. (2019).

1118   A guide to group effective connectivity analysis, part 1: First level analysis with DCM for

1119   fMRI. *Neuroimage*, *200*, 174–190. https://doi.org/10.1016/j.neuroimage.2019.06.031

1120   Zhang, Y., Brady, M., & Smith, S. (2001). Segmentation of brain MR images through a hidden

1121   Markov random field model and the expectation-maximization algorithm. *IEEE Transactions*

1122   *on Medical Imaging*, *20*(1), 45–57. https://doi.org/10.1109/42.906424

1123   Zilles, K., & Amunts, K. (2010). Centenary of Brodmann's map — conception and fate. *Nat. Rev.*

1124   *Neurosci.*, *11*(2), 139–145. https://doi.org/10.1038/nrn2776

1125